AD-A168 449 ACTA AERODYNAMICA SINICA (SELECTED ARTICLES)(U) FOREIGN 1/1
TECHNOLOGY DIV WRIGHT-PATTERSON AFB OH B TONG ET AL.
29 MAY 86 FTD-ID(RS)T-0496-85

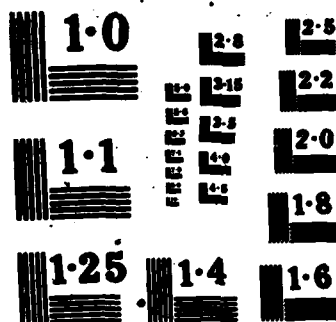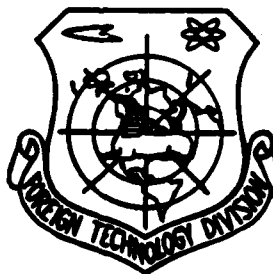UNCLASSIFIED F/G 20/4 NL

NATIONAL BUREAU OF S
MICROCOPY RESOLUTI   TEST

AD-A168 449

FOREIGN TECHNOLOGY DIVISION

DTIC
S ELECTE D
JUN 1 7 1986
D

ACTA AERODYNAMICA SINICA

(Selected Articles)

DTIC FILE COPY

86 6 16 073

HUMAN TRANSLATION

FTD-ID(RS)T-0496-85   29 May 1986

MICROFICHE NR: FTD-86-C-001884

ACTA AERODYNAMICA SINICA (Selected Articles)

English pages: 77

Source: Konggi Donglixue Xuebao, Nr. 3, 1984, pp. 20-41;
        88-109

Country of origin: China
Translated by: SCITRAN
              F33657-84-D-0165
Requester: FTD/TQTA
Approved for public release; Distribution unlimited.

Table of Contents

(Chinese Translations)

i

GRAPHICS DISCLAIMER

All figures, graphics, tables, equations, etc. merged into this
translation were extracted from the best quality copy available.

Accesion For		
NTIS CRA&I		☑
DTIC TAB		☐
Unannounced		☐
Justification		
By		
Distribution /		
Availability Codes		
Dist	Avail and / or Special	
A-1		

QUALITY INSPECTED 3

ii

A Locally Linearized Panel Method
for Calculation of Tri-dimensional
Wing Oscillation Pressure Distribution
at Trans/subsonic Speeds

/20

Tong Binggang   Zhuang Lixian
(Dept. of Modern Mech., Univ. of Sci. & Tech of China)

Li Xianlin
(Computational Center, 5th Inst. of Ministry of Aero. Studies)

ABSTRACT

In this paper, the theory of disturbance potential flow is used as the
basis for a local linear hypothesis to construct a tri-dimensional down-wash
integral equation for wing oscillation at trans/subsonic speeds. The method
for calculation of the trans/subsonic flow Kernel
function is expounded upon. The Generalized Doublet Lattice Method is used
to calculate unstable atmospheric pressure distribution over the rectangular
resonant cavity of an aircraft wing. The results indicated the local method
compared accurately in calculating nonlinear characteristics of unstable flow
forces at trans/subsonic speeds. In regards to calculation of flow forces at
supersonic speeds, more research is required to find a method of numeric
derivation.

I. Foreword

As everyone knows, potential linear flow is often described by means of
a partial differential equation of second order. If the equation is linear,
the fundamental solution is found using repetitive addition. Boundary
conditions for the physical plane may be expressed in the form of an integral

-1-

equation:

$$V_n(x,y,z) = \sum_{i=1}^{2} \frac{\partial}{\partial n} \iint D_i(\xi,\eta,\zeta) K_i(x-\xi, y-\eta, z-\zeta) dS$$

In the formula, S is the solid boundary of the field of flow, added to the interruptive residual surface of the tail. V_n is the velocity derived at plane S. K_i is the fundamental solution to the partial differential equation of the i degree. $D_i dS$ expresses a possible fundamental solution for panel weight of dS. K_i and V_n are pre-determined functions derived from the formula and surface planar conditions. D_i is a possible position within the selection order. The remaining elements deal with certain known functions. After resolving D_i distribution functions, the field of velocity and field of pressure can be expressed integrally as:

$$\Phi(x,y,z) = \sum_{i=1}^{2} \iint D_i K_i dS \tag{2}$$

which gives us a true derivative. For the special case of conditions of the lift plane, we can also obtain an integral equation for extracting load distributions.

The Panel Method of calculation is one of the most important in hydromechanics for finding numeric values.[1] The aforementioned integral equation can be used to extract an accurate representation of flow since it traverses opposing boundary conditions, curved surface boundaries, and odd distributions which begin to depart from theory. Because the definition of

the realm of the integral equation has already degenerated to that of a
curved surface. the computations derived using the integral equation as
compared to direct extraction through a differential equation (Cauchy's Test
for example) fell short. As a result of these problems established in
integral equation (1), the Panel Method proved far superior.

The Panel Method's suitability for solving problems of potential linear
flow under normal and abnormal circumstances, both for non-compressed and
compressed flow, has given rise to its extensive and successful application
[2, 3, 4, 5]. Speaking in regards to small perturbation at transonic flow,
although it has already been proven that the potential flow theory is a very
good approximation, however, because velocity flow equations are nonlinear in
nature, direct application of the Panel Method proved to be very difficult.
This paper used the various proposals set forth by Spreiter on a local linear
theory [6, 7, 8] to construct a panel method for applications of unstable
transonic flow which is called the "Locally Linearized Panel Method." In the
selection of Lissajous's Dispersion Model, this document, in regards to
trans/subsonic flow, proposes the use of a Generalized Doublet Lattice
Method. This method was used for all experimental calculations in order to
clearly demonstrate its effectiveness. As for the criticality of transonic
flow (to include the potential flow in the presence of shock waves) it seems
rational to use Lissajous's Figures as a model for construction, but further
studies are required.

II. A Down-Wash Integral Equation
for Wing Oscillation at Trans/subsonic Speed

In recent years, attention has been towards establishment of a method for
a Kernel function at trans/subsonic speeds, in the western world by
Cunningham, A.M. [9, 10] and _iu, D.D. [11, 12, 13] et al. Cunningham simply
does not use an integral equation based on linear theory, but from within the
Kernel function he makes several adjustments in regards to Mach number
M and frequency K. Liu's method leads into transonic speed acceleration
force, and attempts to establish a velocity acceleration force equation. The
next step leads to a transonic speed down-wash integral
equation. However, we discovered his calculations were in error.
Resultingly, a solution remains unestablished.

As a starting point, this paper devises a local linearized hypothesis
from the force velocity equation for unsteady state small perturbation and
derives a down-wash integral equation for wing oscillation at transonic
speeds. Consider an arbitrary planar surface of non-torsional quality with a
given thickness as the wing. By placing it in the surroundings of a near
sonic horizontal flow influx, the horizontally positioned planar surface
serves as a small scale resonance cavity. As the vibrations reach near
stable conditions, the small perturbation force velocity of flow can be
expressed as:

$$\Phi(x,y,z,t) = \phi(x,y,z) - \varphi(x,y,z)e^{i\omega t}$$

(3)

In this equation, ϕ expresses the wing thickness that gives rise to steady
perturbation force velocity. φ expresses the wing thickness that gives
rise to unsteady perturbation force velocity. Based on the small

perturbation force velocity hypothesis, we have $\phi = 0 \ldots$ and this allows us to formulate the approximation scale equation below:

$$(1 - M_i^2)\phi_{xx} - \phi_{yy} - \phi_{zz} = 0 \tag{4}$$

$$(1 - M_i^2)\varphi_{xx} + \varphi_{yy} + \varphi_{zz} - \frac{2i\omega M}{U}\varphi_x + \frac{M^2\omega^2}{U^2}\varphi = \frac{(\gamma+1)M^2}{U}\phi_{xx}\varphi_x \tag{5}$$

Here, U and M differentiate the inward velocity and Mach number that is the most recent or immediate Mach number value.

$$M_i = M\left[1 + \frac{(\gamma+1)\phi_x}{U}\right]^{1/2} \tag{6}$$

By taking the thickness distribution of the wing and the vibration displacement, the differentiation can be expressed as:

$$z_s = h(x,y) \quad \text{和} \quad z_s = f(x,y)z^{i\omega t} \tag{7}$$

and with equation (4) boundary conditions are expressed as:

$$\left(\frac{\partial\phi}{\partial z}\right)_{z=0} = U\frac{\partial h}{\partial x} \tag{8}$$

while equation (5) expresses the boundary conditions as:

$$\left(\frac{\partial\varphi}{\partial z}\right)_{z=0} = U\left(\frac{\partial f}{\partial x} + \frac{ik}{L}f\right) \tag{9}$$

Herein, $k = \omega L / U$ is the conversion frequency. L is the reference length. Equation (4) is a nonlinear equation, equation (5) is a variable coefficient in linear form. In order to derive these equations, we used the locally linearized hypothesis in all instances. The problem of boundary limits in a differential equation became a related problem in integral equations, so the Panel Method for derivation of numeric values was once again utilized. In regards to the local linearized Panel Method of equation (4), you may reference footnote [14] which discusses in detail a Panel Method of calculation for unsteady state trans/subsonic speed flow oscillation.

According to the locally linearized hypothesis, we can take the coefficients from the various known functions of equation (5). Afterwards, at the proper time, we take these parameters and once again use them as values for the originally known functions. We first discuss $M_i < 1$ pre-conditions for establishment of the trans/subsonic speed flow. With Goethert's transformation

$$x' = x, \quad y' = \beta_i y, \quad z' = \beta_i z; \quad \varphi = \varphi_i e^{\bullet\bullet}$$

(10)

wherein

$$\beta_i = \sqrt{1 - M_i^2}, \quad \alpha = \frac{i\omega M^2}{U \beta_i^2} + \frac{A}{a\beta_i^2}, \quad A = \frac{M^2(\gamma + 1)\phi_{ii}}{U}$$

(11)

and both become constants. Hence, equation (5) becomes

$$\nabla''^2 \varphi_1 + k_1^2 \varphi_1 = 0$$

(12)

In this manner,

$$\nabla''^2 = \frac{\partial^2}{\partial x'^2} + \frac{\partial^2}{\partial y'^2} + \frac{\partial^2}{\partial z'^2}, \quad k_1 = \left(\frac{\omega^2 M^2}{U^2} - a^2 \beta_1^2\right)^{1/2} \Big/ \beta_1$$

(13)

the hypothesis for p, in all respects of continuity, can be differentiated (without shock waves) within the Green formula

$$\iiint (uD^2v - vD^2u)dV_1 = \oiint \left(u\frac{\partial v}{\partial n_1} - v\frac{\partial u}{\partial n_1} \right)dS_1$$

Order $u = (\varphi, x_1', y_1', z_1'), v = e^{-ik_1r''}/r'$, $r' = \sqrt{(x'-x_1')^2 + (y'-y_1')^2 + (z'-z_1')^2}$

and utilization of φ_1 for $z_1' = 0$ plane surface's counter-characteristics, we get

$$\varphi_1(x', y', z') = \frac{1}{4\pi} \iint_{\Sigma'} \Delta\varphi_1(x_1', y_1') \frac{\partial}{\partial z'} \left(\frac{e^{-ik_1r_1'}}{r_1'} \right) dx_1' dy_1'$$

Σ' is $z' = 0$ planar projective surface of the wing and tail flow surfaces. $\Delta\varphi_1$ is Σ' second reading φ_1 difference. Transformed and interpreted via equation (13), it is

$$\varphi(x,y,z) = -\frac{1}{4\pi}e^{\cdots}\iint_{\bar{s}}\Delta\varphi(x_1,y_1)e^{-\cdots}\frac{\partial}{\partial z}\left(\frac{e^{-ik_1 r}}{r}\right)dx_1 dy_1$$

(1?)

where

$$r = \sqrt{(x-x_1)^2 - \beta_1^2[(y-y_1)^2 + (z-z_1)^2]}$$

(15)

and once again the linearized pressure expression

$$p = -\rho_\infty U e^{-\frac{i\omega z}{U}}\frac{\partial}{\partial x}(\varphi e^{\frac{i\omega z}{U}})$$

is utilized. We derive

$$\Delta\varphi(x_1,y_1) = \frac{1}{\rho_\infty U}e^{-\frac{i\omega x_1}{U}}\int_{-\infty}^{x_1}\Delta p(\lambda,y_1)e^{\frac{i\omega\lambda}{U}}\,d\lambda$$

(16)

in the form

$$\Delta p = p_{\text{low}} - p_{\text{up}}$$

and equation (16) is substituted in equation (14) where we have

$$\varphi(x,y,z) = -\frac{1}{4\pi\rho_\infty U}e^{\cdots}\iint e^{-\cdots}\frac{\partial}{\partial z}\left(\frac{e^{-ik r}}{r}\right)$$

$$\left\{\int_{-\infty}^{x_1}\Delta p(\lambda,y_1)e^{\frac{i\omega\lambda}{U}}\,d\lambda\right\}e^{-\frac{i\omega x_1}{U}}\,dx_1 dy_1$$

(17)

Taking the derivative z from the above equations, we can obtain a limit for

$z \longrightarrow 0$. After performing the transformation calculations, it takes the form of a trans/subsonic down-wash integral equation:

$$w_{a} = - \frac{1}{4\pi\rho_{-}U} \iint_{S} \Delta p(x_{1}, y_{1}) K(x-x_{1}, y-y_{1}; \phi_{x}, \phi_{xx}) dx_{1} dy_{1} \tag{18}$$

Here, the Kernal function K takes the specific form of

$$K(x,y) = \lim_{s \to 0} e^{-\frac{i\omega x}{U}} \frac{\partial^{2}}{\partial z^{2}} \int_{-\infty}^{s} e^{(s + \frac{i\omega}{U})t} \left(\frac{e^{-ik_{1}r}}{r} \right) d\xi \tag{19}$$

and $r = \sqrt{\xi^{2} - \beta_{1}^{2}(y^{2} + z^{2})}$.

It is important to point out that the parameters a, a, k_{1}, β_{1}, etc. within K have already used the known functions ξ, y_{1}, originally derived from equation (4) (taking node coordinates x,y as parameters). They reflect that portion of the coupling coefficient of trans/subsonic force velocity's steady state opposing the unsteady state.

In regards to the problem of unsteady states at trans/supersonic speeds, it is possible to apply an integrated method for transformation:

$$x' = x, \quad y' = \beta_{1} y, \quad z' = \beta_{1} z; \quad \varphi = \varphi_{1} c^{\bullet\bullet} \tag{18'}$$

and derive an identical form down-wash integral equation (18). The difference is in the integral equation's dependent domain of nodal regions. The Kernel function's basic form must also be altered to

$$K(x,y) = \lim_{s \to 0} 2e^{-\frac{i\omega x}{U}} \frac{\partial^2}{\partial z^2} \int_{s_{1,r_1}}^{s} e^{(a+\frac{i\omega}{U})z} \, Ch(ik_1 r) \frac{d\xi}{r}$$

(20)

$$r_1 = \sqrt{y^2 - z^2}$$

so

and as $M_1 \approx 1$, we have

$$K(x,y) = \lim_{s \to 0} e^{-\frac{i\omega x}{U}} \frac{\partial^2}{\partial z^2} \int_{0}^{s} e^{(a+\frac{i\omega}{U})z} \; e^{\frac{a+\frac{2}{2}}{4z}} \frac{}{|\xi|} d\xi$$

(21)

So . $a = M_1^2 \omega^2 / a U^2$.

III. The Approximation Calculation of
the Kernel Function for Trans/subsonic Speeds

Deriving the numeric values for the Kernel function of the integral
equation in the Panel Method is a crucial step. Obviously, the Kernel
function's accuracy in calculation (19) is extremely difficult
and we can only make an approximation.
It is for this reason, when solving normal
problems, that we can only figure ϕ_{u}, ϕ_{u} as positions along the aircraft
wing's surface. Moreover, we cannot calculate numeric data for the tail
surface flow. However, with the use of equation (19) we can derive the
necessary figures for normal tail flow as a function value. In the integral
equation $(-\infty, x - x_i)$ are these values (x_i expresses the x-value for the
rear section). However, if we are speaking solely in terms of the normal
tail flow in correspondence to a particular point on the wing's surface, the

x-value representing the tail flow along its planar surface for vibration
rate is indeed very small, in the region of $(-\infty, x-x_1)$ in the integral
equation when using M_∞ to substitute for M_1. Hence, the successful use of
the Kernel function in the integral equation at this stage could be achieved
in linear theory calculation methods (see footnote [5]).

In the Doublet Lattice Method, K is normally altered to become

$$K(x-x_1,\ y-y_1) = \frac{\tilde{K}}{r_1^2} \exp\left[-\frac{i\omega(x-x_1)}{U}\right] \tag{22}$$

and herein we have

$$\tilde{K} = r_1 \frac{\partial I}{\partial r_1}, \quad I = \int_{-\infty}^{x-x_1} \frac{1}{r} \exp\left[\left(a+\frac{i\omega}{U}\right)\xi - ik_1 r\right] d\xi \tag{23}$$

$$r_1 = \sqrt{(y-y_1)^2 + z^2}$$

and is like

$$I = I_1 - I_2 = \int_{-\infty}^{x-x_1} (\cdots) d\xi - \int_{x-x_1}^{\infty} (\cdots) d\xi \tag{23b}$$

$$\tilde{K}_1 = r_1 \frac{\partial I_1}{\partial r_1}, \quad \tilde{K}_2 = r_1 \frac{\partial I_2}{\partial r_1}$$

where we obtain

$$\tilde{K}_1 = -\int_{x_1}^{\infty} \frac{e^{-ik_1 u}}{(1+u^2)^{3/2}}\ du + \frac{M r_1 e^{-ik_1 u_1}}{R\sqrt{1+u_1^2}} \qquad (r_1 \neq 0) \tag{24}$$

so we have

$$k_i = \frac{\omega r_i}{U}, \quad u_i = -\frac{(x-x_i)-MR}{\beta_\infty^2 r_1}, \quad R = \sqrt{(x-x_i)^2 + \beta_\infty^2 r_1^2} \tag{24c}$$

and the numeric values of equation (24) are calculated in a very convenient manner [5],

$$\tilde{K}_i = -ir_i^2 \int_{s-x_i}^{s-x_1} \frac{k_i \beta_i^2}{r^2} \exp\left[\left(a + \frac{i\omega}{U}\right)\xi - ik_i r\right] d\xi$$

$$-r_i^2 \int_{s-x_i}^{s-x_1} \frac{\beta_i^2}{r^2} \exp\left[\left(a + \frac{i\omega}{U}\right)\xi - ik_i r\right] d\xi \tag{25}$$

Now we can use a problem relating to stable characteristics with a low frequency development (K << 1) and take these small small values to use as exponents for our function values. This will give us a start and make the calculation of equation (25) much more convenient. Just as we get to the third stage, we get

$$\tilde{K}_i = F(x_1) - F(x_i), \quad (r_i \neq 0) \tag{26}$$

where the function F is defined as

$$F(\lambda) = \frac{\beta_i^2(\lambda) r_i^2}{r(\lambda)} [(x-\lambda) + r(\lambda)]^{-1}$$

$$+ \frac{\beta_i^2(\lambda) r_i^2}{r(\lambda)} \left[a(\lambda) + \frac{i\omega}{U}\right]\left[1 + \frac{1}{2}(x-\lambda)\left(a + \frac{i\omega}{U}\right)\right] \tag{27}$$

$$- \frac{\beta_i^2(\lambda) r_i^2}{2}\left\{\left[a(\lambda) + \frac{i\omega}{U}\right]^2 + k_i^2(\lambda)\right\}\left\{\frac{x-\lambda}{2r(\lambda)}\right.$$

$$\left. + \frac{\beta_i^2(\lambda) r_i^2}{2[(x-\lambda)+r(\lambda)]r(\lambda)} + \ln[(x-\lambda)+r(\lambda)]\right\}$$

and in it is

$$r(\lambda) = [(x-\lambda)^2 - \beta_i^2(\lambda) r_i^2]^{1/2} \tag{27a}$$

so as $r_i = 0$, a separation of the odd nodal points at the rear crux occurs and

from our Kernel function we have

$$\begin{cases} \bar{K}_1 = 0 \\ \bar{K}_2 = \begin{cases} 0 & \text{当 } x < x_1 < x_2 \text{ 时} \\ -2 & \text{当 } x_1 < x < x_2 \text{ 时} \end{cases} \end{cases} \qquad (r_1 = 0)$$

(28)

IV. Analysis of Calculations
and Final Conclusions

Wh have calculated the perturbation pressure distributions of near son :
speed flow ($M_\infty = 0.7, 0.8$) for rectangular wing oscillation. The
thickness of the wing was obtained at a 5% ratio of the double circular arc
cross section; the str... ratio was 8%. The oscillation frequency rate was
$k = \omega b / U = 0.17$,   and b was taken as a mid-wing spread. The vibration model
was a symmetrical axis (the x-axis) with resonance at the first
winding:

$$\frac{w}{U} = i \frac{\omega}{U} h (0.18043 \bar{y} - 1.70255 \bar{y}^{1} - 1.13683 \bar{y}^{1} - 0.25387 \bar{y}^{1})$$

(29)

Here, $\bar{y}$ = y/b. Normal flow distribution was calculated in accordance with
the methods outlined in footnote [14]. Abnormal flow measurements were taken
using the Generalized Doublet Lattice Method for calculation. $h\omega/U$ was
obtained at a specific point as the amplitude C for the pressure coefficient.
 Using different cross sections (y = a constant value) for $|C_p| \sim x$ and $\phi \sim x$
curvilinear surface. ϕ becomes the phase angle. In order to make a

comparison, the charts found in footnote [15] are provided as a contrast to the experimental numeric data and the results of a linear theory approach.

Figure 1 and Figure 2 represent unstable pressure curves when M=0.7. It is clear in Figure 1 that when M=0.7 this method's calculation of C in curvilinear measurements and numeric data is much better, especially along the forward half of the wing. Theory and experimental results were in accord with each other. However, when using the linear theory to obtain results, there was a great disparity that was quite obvious. Figure 2 expresses a phase curve that clearly shows a discrepancy between theory and experimental results,especially for the vicinity of the exterior strain measurements for 3/4 of the wing. Footnote [15] makes a further comparison and in-depth explanation. It must be pointed out that these discrepancies were at M=0.7 conditions, which includes wing oscillation and the effects of wind-caused vibration.

Figure 3 illustrates $|C_p|{\sim}x$ as a curvilinear surface when M=0.8 (near Mach number boundary) for the local method. At the same time, it also provides conditions for M=0.7 and M=0.9,from the experimental results of footnote [15]. For both of these represented conditions, we used averaged numeric values. Of course, this comparison is not one of theories, but is provided just to serve as a reference point because the flow at M=0.9 is clearly a shock wave. However, as a reference it is very obvious to see the experimental results coincide with theoretical for the forward portion of the wing. For the rear section of the wing, however, there is a large discrepancy between theory and experimental results. This is because $C_p|_{max}$ under these conditions is influenced by the shock wave

of the wing. We used "averages" here in order to make a relevant comparison.
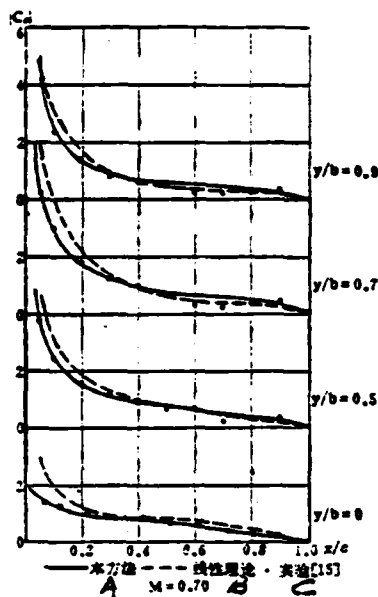

Figure 1

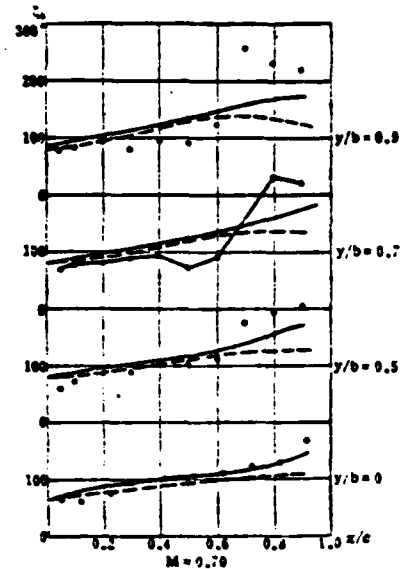Key: a - this method; b - linear theory; c - test results

Figure 2

In summation, we can make the following conclusions: this paper proposed a local linearized trans/subsonic speed oscillation down-wash integral equation as well as the Generalized Doublet Lattice Method for trans/subsonic speed flow. It is possible to calculate at small widths the small perturbation amplitudes.for the wing's planar surface pressure distribution. It is also possible for reactions to occur at transonic flow in an indiscriminate manner for nonlinear forms. This is why the method is superior to that of linear theory. If we should use a blend of (19), (20), and (21) for our Kernel function, the original data values can provide a numeric foundation for calculation of trans/subsonic flow. However, if the theory could be designed in a manner to effectively incorporate Lissajous's Figures, it would advance us a step further in more profound research.
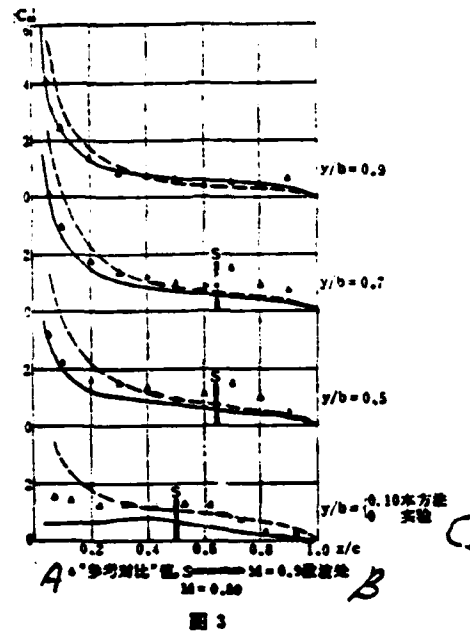
Figure 3
Key: a - "reference comparison" data; b - shock wave
field; c - test results for this method

If shock waves are manifest from the wing's planar surface, it is necessary

and proper to include the relationship of these waves, as well as their

interval. The unsteady state down-wash integral equation handles this

nicely. In normal problem solving, it is difficult to ascertain under what

circumstances it is best to use the Panel Method to accurately determine the

point from which shock waves manifest, or its type and characteristics. At

this point, it would be difficult to speculate further.

[1] Hunt, B., "The panel Method for Subsonic Aerodynamic flows", 载于 Kollmann, W. 主编, "Computational Fluid Dynamics", pp 99—166, McGraw-Hill 1979.

[2] Hedman, S. G., FFA, Rep. 105 1965.

[3] Hess, J. L. & Smith, A. M. O., Progress in Aeronautical Sciences, Vol. 8, Pergamon, London (1967).

[4] Ruobert, P. E. et al., The Boeing Co.-Report, D6-15047-1 (1967).

[5] Rodden, W. P. et al., AGARD-CP-80-71, No. 4 (1971).

[6] Spreiter, J. R. & Alksne, A. Y., NASA Rep. 1359 1953.

[7] Spreiter, J. R. & Alksne, A. Y., NASA TR R-2 1959.

[8] Stahara, S. S. et al., NASA CR 2258 1974.

[9] Cunningham, A. M., NASA CR-144895 1975.

[10] Cunningham, A. M., AIAA Paper No. 74-359 1974.

[11] Liu, D. D. et al., AGARD CPP-227, No. 12 1977.

[12] Liu, D. D et al., AFFDL-TR-79-3055 1979.

[13] Pi, W. S. et al., AIAA 79-0075 1979.

[14] 童秉纲、庄礼贤、李贤淋, "三维厚翼机翼上亚音临界定常液压力力分布的面元迭代解", 空气动力学学报, 2(1984).

[15] Lessing, H. C. et al., NASA TND-344 1960.

A LOCALLY LINEARIZED PANEL METHOD FOR TRAN-/ SUBSONIC FLOW PAST AN OSCILLATING WING

Tong Bingang, Zhuang Lixian

Dept. of Modern Mech., Univ. of Sc. & Tech. of China

Li Xianlin

Computation Centre, The 5-th Institute of the Ministry of Aerospace Industry.

Abstract

In this paper, the down-wash integral equation for the small perturbation transonic potential flow past an oscillating wing is established on the basis of local linearization concept. The method for calculating the tran-/subsonic kernel function is discussed in detail. To calculate the unsteady pressure on an oscillating rectangular wing in the tran-/subsonic flow, the generalized-doublet-lattice-method is used. The results show that the locally linearized panel method is more accurate than the usual linearized methods. But further efforts are needed so as to obtain a numerical method available for calculating the tran-/supersonic flows.

PRESSURE INTENSITY DISTRIBUTION COMPUTATION FOR A FLEXIBLE WING AT TRANSONIC SPEED

Shen Kewyang, Zhuang Xihua
(Shanghai Aviation Industry Corporation)

ABSTRACT

$\underline{L\,28}$

This document utilizes an iterative problem
solving method to calculate pressure intensity dis-
tributions of a flexible wing at transonic speeds.
A second order approximation method is used to derive
aerodynamic force for small perturbation potential
flow at transonic speed; a one-dimensional single
beam theory or a two-dimensional surface structure
matrix is used to calculate a flexion coefficient of
effect. All results shown are for the calculations
of a M6 flexible wing. The calculation methods for
the iteration number of the flexible wing and the
rigid wing are the same. Flexion change for wing
surface aerodynamic force load distribution and
shock wave intensity is clearly influenced.

I. Foreword

As all of us know, aircraft wing flexion change has a very
important influence on aerodynamic force load distributions. In
transonic speed computations, because of the nonlinear character-
istics of the fundamental equation, a solution for aerodynamic
force is obtained through an iterative method. As a result of
this, the basic line of thought for obtaining a solution for
transonic speed wing flexion aerodynamic force was as follows:

during the course of obtaining an iterative solution for aero-
dynamic *force*, an interruption in the sequenced non-convergent
aerodynamic load calculations for structural change occurred.
Moreover, the quantitative change computed during the course of
calculation of iteration for aerodynamic force showed a direct
convergence. According to this reasoning, Chipman, et al., [1]
used the low relaxation method of iteration to create an equation
for computation of structural change at transonic speed small
perturbation and obtained convergence for a flexible wing's aero-
dynamic force at transonic speed. Whitlow, et al., [2] took
this method and created a generalized applied equation for deri-
vation of velocity potential at transonic speed.

This paper utilized the transonic speed derivation of higher
order equation (TSDH) to solve for aerodynamic force. Structural
change is calculated using the one-dimensional simple beam model
or the two-dimensional surface matrix for calculation of a flexion
coefficient of effect. All results shown herein are for calcula-
tion of an M6 flexible wing and they have gone through approxi-
mately 100 iterative derivation trials for the obtained conver-
gence of structural change and pressure intensity distributions.
At the same time, calculations revealed flexion change at tran-
sonic speed was clearly influenced by the aerodynamic forces.

II. Calculation methodology

After designating the influx Mach number as M_∞ and designating
velocity pressure as q, as well as specification of the wing
surface conditions, the aerodynamic force distribution $\{L\}$ in
small perturbation theory is merely a function of sectional over-
lap angle distribution $\{\alpha\}$ and sectional slope $(\partial y_u/\partial x)_{u,l}$, so

$$\{L\} = f(\{P\}) \tag{1}$$

In the equation P is substituted for α or $(\partial y_u/\partial x)_{u,l}$, and here
lower point u,1 is separated to indicate upper and lower wing
surfaces. P can only be expressed as

$${P} = {P_R} + {P_L}$$

<div align="right">(2)</div>

In this equation, P_R expressed the values of rigid characteristics and P_E expresses the contributions of structural change. ${P_E}$ is merely a function of aerodynamic force ${L}$, so

$${P_E} = g({L})$$

<div align="right">(3)</div>

An iteration method can be used to solve this group of nonlinear equations. This paper uses the low relaxation method of iteration for calculation of structural change, so

$${P_E}^{(n+1)} = {P_E}^{(n)} + \omega [g({L}^{(n)}) - {P_E}^{(n)}]$$

<div align="right">(4)</div>

/2!

In the equation (n) and (n+1) distinguish the various iteration values for n trials and n+1 trials; ω is a factor of the low relaxation method and is set at $\omega = 0.75$.

1. Model for aerodynamic force

The fundamental equation for the calculation of aerodynamic force at transonic speed is the TSDH equation

$$\left[1 - M_\infty^2 - (\gamma+1)M_\infty^2 \varepsilon \varphi_x - \frac{\gamma+1}{2}M_\infty^2 \varepsilon^2 \varphi_x^2\right]\varphi_{xx} + [1-(\gamma-1)M_\infty^2 \varepsilon \varphi_x](\varphi_{yy} + \varphi_{zz})$$

$$-2M_\infty^2(1+\varepsilon\varphi_x)[(a+\varepsilon\varphi_z)\varphi_{xz} + \varepsilon\varphi_z\varphi_{zz}] = 0, \quad [x \neq x_{LE}(z)]$$

<div align="right">(5)</div>

The corresponding wing surface boundary conditions are expressed as

$$\varepsilon\varphi_y(x, \pm 0, z) = f_c\left\{\left(\frac{\partial y_u}{\partial x}\right)_{u,l}[\cos\alpha + \varepsilon\varphi_x(x, \pm 0, z)] - \sin\alpha\right\}, \quad [x \neq x_{LE}(z)]$$

<div align="right">(6)</div>

In the equation, ε is a parameter for small perturbation, $\varepsilon = \delta^2/M_\infty$, δ is mean correlational thickness of the wing. φ is the small perturbation velocity potential. γ is the comparative specific heat, f_c is an adjustment coefficient, $f_c = M_\infty^{1/4}(M_\infty < 1$ time) (TN: here time may refer to measured unit or trial). In the obtuse forward peripheral area of $x = x_{LE}(z)$, boundary conditions are

$$\varphi_{x_{LE}} = \varphi_{z_{LE}} \cdot \text{tg} \cdot l_{LE} - \frac{\cos\alpha}{\varepsilon}, \quad [x = x_{LE}(z)]$$

<div align="right">(7)</div>

In this equation, l_{LE} is the reverse angle of the forward periphery. The obtuse forward peripheral potential velocity equation is

<div align="center">-20-</div>

$$\left[1-\left(\frac{\text{tg}\,\varLambda_{LE}\,\varepsilon\varphi_{,LE}}{a^*}\right)^2\right]\varphi_{ss}+\left[1-\left(\frac{\varepsilon\varphi_{,LE}-\sin\alpha}{a^*}\right)^2\right]\varphi_{yy}-\left[1-\left(\frac{\varepsilon\varphi_{,LE}}{a^*}\right)^2\right]\varphi_{ss}$$

$$-2\text{tg}\,\varLambda_{LE}\left(\frac{\varepsilon\varphi_{,LE}}{a^*}\right)^2\varphi_{ss}-2\text{tg}\,\varLambda_{LE}\left[\frac{\varepsilon\varphi_{,LE}(\varepsilon\varphi_{,LE}-\sin\alpha)}{a^{*2}}\right]\varphi_{sy} \qquad (8)$$

$$-2\frac{\varepsilon\varphi_{,LE}(\varepsilon\varphi_{,LE}-\sin\alpha)}{a^{*2}}\varphi_{yy}=0\;,\;\{x=x_{LE}(z)\}$$

and the equation

$$a^{*2}=M_z^2+\frac{\gamma-1}{2}\left[1-\left(\frac{\varepsilon\varphi_{,LE}}{\cos\varLambda_{LE}}\right)^2-(\varepsilon\varphi_{,LE}-\sin\alpha)^2\right] \qquad (9)$$

By utilizing all of the difference schemes provided in
bibliographical reference [3] for the equations (5)-(8), dis-
cretization for the difference equation group may occur.
Furthermore, after using the scarce density mesh substitution
iteration method to obtain a result for velocity potential ϕ
convergence, the wing surface pressure intensity coefficient C_p
can be used for calculation in the formula below:

$$C_p=\frac{2}{\gamma M_z^2}\left[\left\{1-\frac{\gamma-1}{2}M_z^2(2\varepsilon\varphi_x+\varepsilon^2\varphi_x^2+2a\varepsilon\varphi_y+\varepsilon^2\varphi_y^2+\varepsilon^2\varphi_z^2)\right\}^{\frac{\gamma}{\gamma-1}}-1\right] \qquad (10)$$
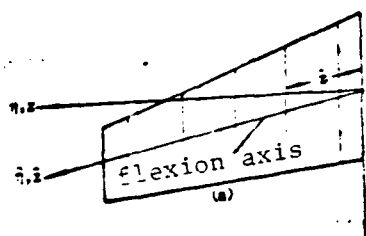
2. Structural model

(1) One-dimensional simple beam model for a long, tapered
wing. We can use the one-dimensional simple beam (flexion axis)
theory to calculate a sectional overlap angle for elasticity [4].
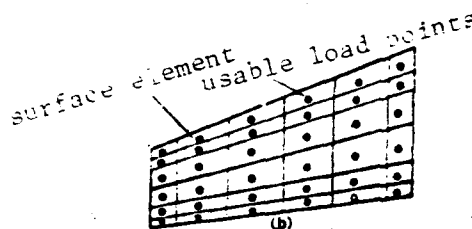
$$a_\varepsilon(\hat{z})=\int_0^z\frac{m(\hat{z},\hat{\eta})M(\hat{\eta})d\hat{\eta}}{EI(\hat{\eta})}+\int_0^z\frac{t(\hat{z},\hat{\eta})T(\hat{\eta})d\hat{\eta}}{GJ(\hat{\eta})} \qquad (11)$$

In the equation, $a_\varepsilon(\hat{z})$ is the sectional overlap angle for elas-
ticity in $\hat{z}$. $m(\hat{z},\hat{\eta})$ is the unit moment of force produced for the
curve distribution. $M(\hat{\eta})$ is the aerodynamic force load and
inertial load distribution {L} along the curve. $EI(\hat{\eta})$ is the distri-
bution of curve rigidity along the edge of the flexion axis.
$t(\hat{z},\hat{\eta})$ is the torsional distribution produced by the unit moment /30
of force within $\hat{z}$. $T(\hat{\eta})$ is the aerodynamic load {L} and the
inertial load's torsion distribution. $GJ(\hat{\eta})$ is the distribution
of torsional rigidity along the flexion axis. As is outlined

-21-

in Figure 1(a), lift $\{L\}$ for each of the wing sectional plate
components perpendicular to the z axis can be obtained with
integral equation (10). Next, by using equation (11), we can
calculate each plate's flexion overlap angle $\{a_f\}$,

(a) one-dimensional simple   (b) two-dimensional surface
beam (flexion axis) model.   structural model.

Figure 1. Structural models of aircraft wing

(2) Two-dimensional surface structural model. As is out-
lined in Figure 1(b), finite trapezoidal elements are divided
into specific pressure regions on the wing surface. Through
theoretical calculations or experimentation, a coefficient of
effect $[C'']$ for flexion is obtained for each surface element.
Hence, the quantitative form transformation is represented as

$$\{y_f\} = [C'']\{F\} \tag{12}$$

In the equation, $\{F\}$ is the usable amassed load of the form

$$\{F\} = \{\Delta C_P - f_I\} s\} q \tag{13}$$

In this equation, ΔC_p is obtained from equation (10) for aero-
dynamic force differences (the upper orientation). f_I is used
for the form's inertial load density (the lower orientation).
s is the surface of the finite element. Thus, the arising
changes of the wing structure, partitioned into upper and lower
slope surface areas are

$$\left\{\left(\frac{\partial y_v}{\partial x}\right)_f\right\}_{v,i} = \frac{\partial \eta_f}{\partial x} \tag{14}$$

In this manner, through use of equation (11) or equation
(14), we can obtain a value for $\{P_E\}$ for use in equation (2).
In computation, for each iteration of aerodynamic force m times

(for loose mesh, m = 10; for packed mesh, m = 5), it is convenient to use equation (11) or equation (14) to figure $\{P_E\}$ initially. After obtaining a value for $\{P\}$ in equation (4) using the low relaxation method, the value can then be substituted in equation (6) to calculate the next m iterations of aerodynamic force until the aerodynamic force and the value $\{P_E\}$ both converge.

III. Calculation results and discussion

In order to test the feasibility of this method, we selected known finite rigidity results for an M6 wing (M_∞ = 0.84, α = 3.06°) [3] as a calculation model. We used a 1/2 wing spread value of 7.41 meters, influx velocity pressure q was 5128 kg/m^2. The flexion axis was at a 50% tension field, the curve rigidity distribution EI is shown in Figure 2. Torsional rigidity was not figured in the calculation. In regards to the two-dimensional structural model, the flexion coefficient of effect is calculated using the equation below:

$$C''(\hat{z},\hat{\eta}) = \int_{0}^{\bar{z}} \frac{(\hat{\eta}-\hat{\lambda})(\hat{z}-\hat{\lambda})}{EI(\hat{\lambda})} d\hat{\lambda} \tag{15}$$

In this integral, the upper limit $\bar{z}$ is $\hat{\eta} \geqslant \hat{z}$ when $\bar{z} = \hat{z}$, and when $\hat{\eta} \leqslant \hat{z}$ it is $\bar{z} = \cdot$.

The following are calculation conditions for the model:

(1) Flexible wing M6E1 (α = 3.06°)--M_∞ =0.84, α = 3.06°. In regards to the influence of pressure intensity distributions, we must understand the overlap angle does not change as flexion change takes place. E1 expresses use of the simple beam theory in equation (11) for the calculation of flexion overlap angle.

(2) Flexible wing M6E1 (α = 5.2°) --M_∞ =0.84, α = 5.2°. This is the flexible wing's lift and the origin for rigid wing M6 comparisons. In regards to the influence of pressure intensity distributions, we must understand that lift does not change as flexion change takes place.

-23-

(3) Flexible wing M6E2 (α = 3.06°)--M_∞ = 0.84, α = 3.06°. E2 expresses a two-dimensional flexion matrix used in equation (2) to calculate structural change. This calculation process uses the data of the two-dimensional structural model to postulate reasonable possibilities for our method. Furthermore, the calculated results are comparable to those for M6E1.

The results of these calculations are illustrated in Figures 3-6. The iterative calculation process converges on the objective $E = \mathrm{MAX} |\varphi_i^{(n)} - \varphi_i^{(n-1)}| \leqslant 10^{-3}$. Bibliographical reference [5] further expands upon the results of this experimental objective, and it provides wind tunnel data to coincide with it.

Figure 3(a) expresses the wing flexion overlap angle a_E for M6E1 under conditions of change as an iteration number over n trials. As you can see, stability increases with an increase in the change in the iteration number. The change for M6E2 is also likewise. Figure 3(b) expresses the wing flexion overlap angle a_E for changes that occur in η. As the figure clearly shows, a two-dimensional structural model's flexion axis deflection curve is obtained by the flexion overlap angle and is close to the results for M6E1, so we have

$$a_E = -\sin \Lambda \frac{dy_E}{dz}$$ /32

in the formulae, Λ is the flexion axis reverse sweep angle, dy_E/dz is the slope change for the flexion axis along the flexion axis deflection surface.

Figures 4 and 5 differentiate results of chord direction for pressure intensity distributions, sectional lift coefficient C_y, and the sectional pressure point x_d for three aforementioned models. Furthermore, these results are compared to the results for M6. As you can see in the figure, aerodynamic force flexion, aside from the serious influences of lift distribution, is clearly influenced by pressure intensity distributions and shock wave intensity. At the same time, the closeness of results for M6E1

-24-

($\alpha = 3.06°$) and M6E2 ($\alpha = 3.06°$) remained true for all mathematical theory methods tried in experiments for a two-dimensional structural model.

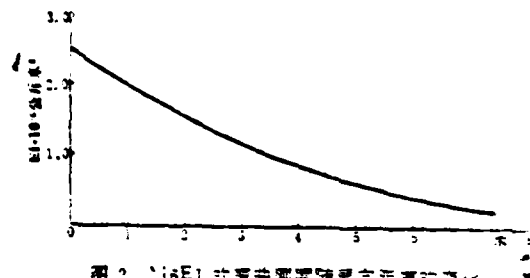图 2. M6E1 的弯曲刚度随展向距离的变化

Figure 2. M6E2 curve rigidity coinciding to matrix changes.
1--$E1*10^{-3}$ kg/m; 2--meters

---- M6E1 ($\alpha = 5.2°$)
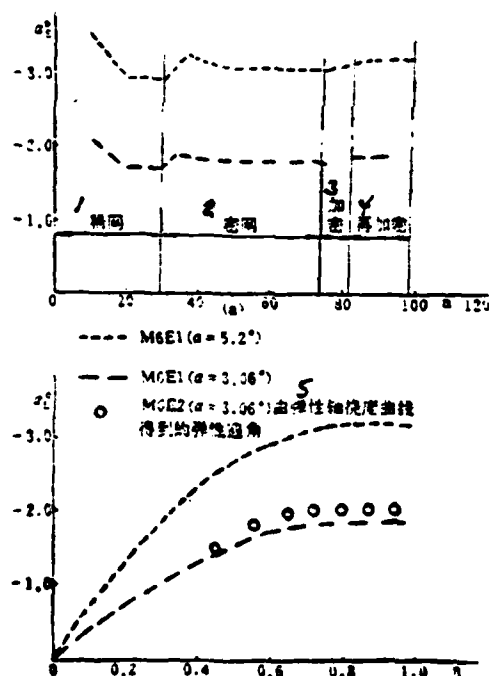— M6E1 ($\alpha = 3.06°$)
o M6E2 ($\alpha = 3.06°$)由弹性轴挠度曲线得到的弹性迎角

Figure 3. Structural change coinciding with wing change and iteration number.
1--loose mesh; 2--packed mesh; 3--increased density; 4--even more increased density; 5--M6E2(a=3.06°) via flexion axis deflection curve of obtained flexion overlap angle.

M6 ($\alpha = 3.06°$)
M6E1 ($\alpha = 5.2°$)
+ × M6E1 ($\alpha = 3.06°$)
• M6E2 ($\alpha = 3.06°$)

$C_p = -0.327$

(a) $\eta = 0.2$

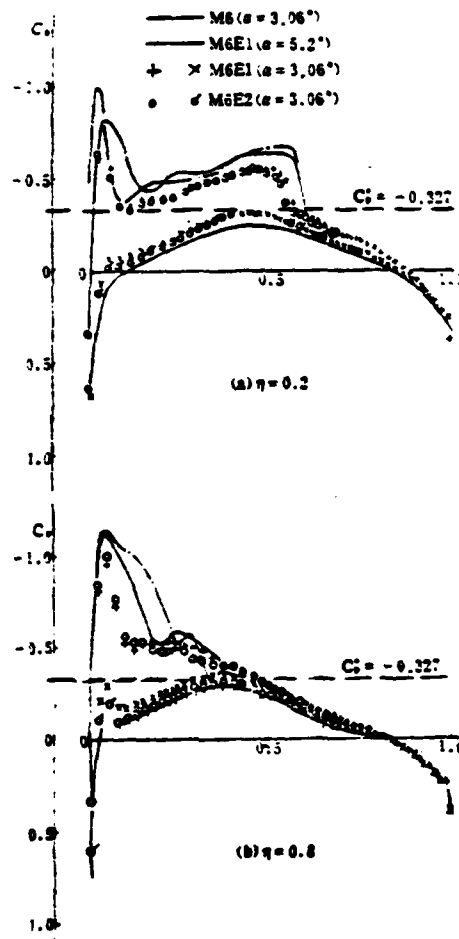$C_p = -0.327$

(b) $\eta = 0.8$

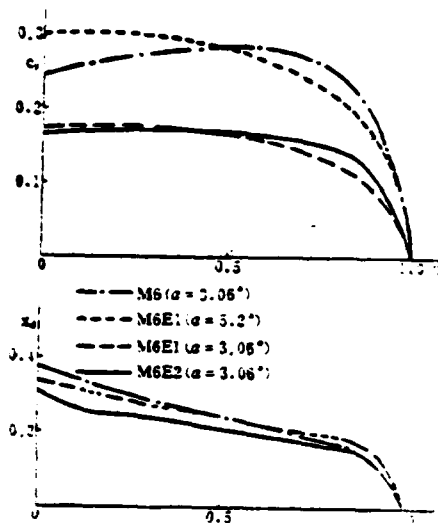Figure 4. Comparison of pressure intensity computation results.

Figure 5. Comparisons of sectional lift coefficients and relative pressure.

TABLE 1. Aerodynamic force derivative comparisons

气动导数[1]	M6	M6E1/M6E2	$K = \frac{弹性值}{刚性值}$[2]
C_y^A·1/度[3]	0.0844	0.0431	0.570
m_z^a·1/度	-0.0622	-0.0334	0.537

1--aerodynamic derivative; 2--k=flexion value/rigidity value; 3--1/degrees

TABLE 2. Iterative trial comparisons ($E=10^{-3}$)

表 2 迭代次数比较($E=10^{-3}$)

情况[1]	M6	M6E1 $\alpha=3.06°$	M6E2 $\alpha=3.2°$	M6E2 $\alpha=3.06°$
n	93	91	98	115

1--conditions

Finally, Table 1 shows how aerodynamic force flexion is influenced by linear slope of lift C_y^A and derivative M_z^a for the pitching moment. The table shows a significant difference for M6E1 and M6E2. Table 2 shows comparisons for the iterative number.

As you can see, the iteration numbers for a flexible wing and a rigid wing are nearly equal. Resultingly, the flexible wing transonic speed computations take about the same amount of time to figure as for a rigid wing, using less than one hour of CPU time on an IBM 4341 computer.

IV. Conclusions

For the nonlinear nature of near transonic speed aerodynamic force computations, this paper in the course of iterative deriva-tion for aerodynamic force, interrupts the computation of the aerodynamic force based on its previously obtained values for structural change, then these values for quantitative change are placed into the iteration process for aerodynamic force until they

converge. For the scope of M6 flexible wing calculations shown herein, this computation method proved quite effective in finding solutions for a flexible wing's quantitative change and aerodynamic force distribution convergence. Because of this, the method cited herein can be used to predict the aerodynamic force and flexion for the lift plane at transonic speed as well as to predict aerodynamic flexion cuts in the lift surface design.

REFERENCES

[1] Chipman, R., Waters, C., Mackenzie, D. Numerical computation of aeroelastically corrected transonic loads, AIAA, 79-766.

[2] Whitlow, W. Jr., Bennett, R. M. Application of a transonic potential flow code to the static aeroelastic analysis of three-dimensional wings, AIAA 82-689.

[3] Shen Keyang. Two-dimensional approximation method for swept wing aircraft at transonic speed circular flow, Journal of Aviation and Space, 4,4(1983), 1-10.

[4] Gray, W. L., Schenk, K. M. A method for calculating the subsonic steady-state loading on an airplane with a wing of arbitrary plan form and stiffness, NACA TN 3030 (1953).

[5] Zhang Xihua, Shen Keyang. Transonic speed pressure intensity distribution computations for 60° Delta wings at M = 0.94 and 0.98, 2nd National Computative Fluid Mechanics Conference (1984).

TRANSONIC PRESSURE DISTRIBUTION COMPUTATIONS
OF A FLEXIBLE WING

Shen Keyang, Zhang Xihua
Shanghai Aviation Industry Corporation.

Abstract

An iteration method is used for computing the transonic pressure distribution on a flexible wing. The aerodynamic force is solved with the second order approximation method for transonic small disturbance potential flow. The structural deflection is computed using the one-dimensional simple beam theory or a two-dimensional flexibility matrix method. The typical computations for M6 flexible wing indicate that the iteration number for flexible wing computation is only slightly more than that for rigid one, and that the influences of the structural deflection on the airload and shock strength are important.

ON RELAXATION OF TRANSONIC VELOCITY ZERO LIFT AIRFOIL
POTENTIAL FLOW AND CONVERGENCE OF TWO SELF-CORRECTING
WIND TUNNELS

Liu Xueding, Luo Shijun
(Northwestern Polytechnical University)

ABSTRACT

This document utilizes a transverse small per-
turbation velocity potential equation or a longitu-
dinal large perturbation velocity potential equation
to calculate the potential flow for a zero lift
airfoil at transonic velocity. In numeric line
relaxation testing [1], when the ϕ_x difference equa-
tion uses a simple iteration methodology and when the
ϕ_{xx} difference equation uses an improved iteration
methodology, the characteristics of stability compare
favorably.   This conclusion coincides with the
theoretical analysis of linearization cited in biblio-
graphical reference [2].

This document uses a mixed difference method of
numeric simulation to verify the static pressure
along the wing surface in regards to a two control
surface for convergence of zero lift airfoils in a
self-correcting wind tunnel at transonic velocity.
For the former scheme, a NACA 0012 airfoil is used,
$M_\infty = 0.9$ and a RAE 104 airfoils is used, $M_\infty = 0.8$.
In regards to the former scheme, a NACA 0012 airfoil
is used, $M_\infty = 0.72, 0.8$. When the stream angle is at
zero and wind tunnel height is comparable to wing
chord, we can nearly get a convergence of free flow
with no wind tunnel wall interference after about
three hours.

When using the mixed difference line relaxation method to solve transonic potential flow equations, we ran into a problem with convergence. The majority of computation experiments [1] revealed the following: during calculations involving super-critical flow, the iteration method caused a problem that influenced the stability for convergence. This document discusses the problem and the experimental test results which turned out to be significant for it.

Bibliographical reference [3] cites a self-correcting method that uses two airflow parameters ϕ_x and ϕ_y for a one control surface. Numeric simulation proved that when supercritical flow manifests itself within the field of flow for the NACA 65A003 airfoils, the self-correcting wind tunnel converged. Considering the difficulties of obtaining a measurement of ϕ_y in wind tunnel experiments, this document proposes that only two measurements, for static pressure and ϕ_x, need to be done in the self-correcting wind tunnel scheme. The convergence was proven in this manner by utilizing numeric simulation.

I. An iteration method for the influences of convergence

Consider a normal surface potential flow at transonic speed. The hypothetical orientation perturbation velocity y, as compared to the last crossed perturbation velocity of q_∞ is much less. However, the x orientation perturbation velocity has the possibility of not being less. Perturbation velocity can be adequately represented in a partial differential equation as

$$(1-M')\varphi_{xx}+\varphi_{yy}=0 \tag{1.1}$$

and in the formula

$$1-M'=\frac{1-M_\infty^2-\frac{\gamma+1}{q_\infty}M_\infty^2\varphi_x-\frac{\gamma+1}{2q_\infty^2}M_\infty^2\varphi_x^2}{1-\frac{\gamma-1}{q_\infty}M_\infty^2\varphi_x-\frac{\gamma-1}{2q_\infty^2}M_\infty^2\varphi_x^2} \tag{1.2}$$

y is the airflow's adiabatic index number, M_∞ is the last crossed Mach number for perturbation airflow.
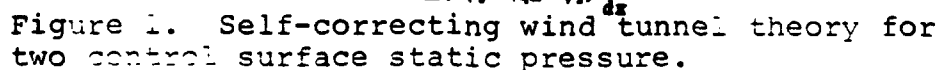
Equation (1.1) is a mixed form nonlinear equation. Due to the multi-faceted nonlinear characteristics of the group of equations as seen in (1.1), we can use a line relaxation iteration method to linearize a solution. As the edge of the y axis orients towards line relaxation, an iteration equation is required for the velocity discriminant $1-M^2$, ϕ_{xx} coefficient and the various ϕ_{xx} values of velocity potential apart from the relaxation line.

According to page 62 of [4], an accurate difference scheme for velocity discriminants can, on the one hand, use a simple iteration, but for supercritical airflow, this can lead directly to a divergence of vibration. This can be organized into several iterative methods as cited below:

$$
\text{velocity discriminant} \; \underline{1-M^2 \text{ simple iteration}} \left|
\begin{array}{ll}
\phi_x \text{ simple iteration,} & \phi_{xx} \text{ simple iteration } (P = 0) \\
\phi_x \text{ improved iteration,} & \phi_{xx} \text{ improved iteration } (P = 1) \\
\phi_x \text{ simple iteration,} & \phi_{xx} \text{ improved iteration } (P = 2) \\
\phi_x \text{ improved iteration,} & \phi_{xx} \text{ simple iteration } \quad (P = 3)
\end{array}
\right.
$$

Numeric experimentation [1] revealed the following information: for $M_\infty < 0.775$ free flow, for use of the $P = 0$, 1 and 2 iterative methods, the calculations approximated convergence. The only difference was in the speed at which convergence occurred. For $M_\infty \geq 0.8$ free flow, the supposed local supersonic region was relatively large, and an intense shock wave manifested. Using the two iterative methods $P = 0$, 1, it was extremely difficult for a convergence to occur in computation. However, using the iteration method with $P = 2$, a calculation result that systematically led to success with M_∞ was obtained. The greatest value for M_∞ was about 0.925. With a 39x23 mesh, the Ximen 7760 computer took about 10 minutes to perform the calculations. This goes to say that the iteration method for $P = 2$ are one way to use computations of supercritical flow to make comparisons of stability. The theory and results of this discussion is analyzed in [2]. Based on [2], the simple iteration method for ϕ_{xx} localized supersonic points is unstable. For the condition of $P = 3$, this paper performed no experiments or calculations.

II. Self-correcting wind tunnel convergence for zero lift symmetric airfoils in view of static pressure at transonic speed for two control surfaces

This document uses the same airflow parameters ϕ_x static pressure for two control surfaces in the self-correcting wind tunnel. The proofs given are in regards to the NACA 0012 airfoil RAE 104. When supercritical flow manifests within the field of flow, there is convergence within the self-correcting wind tunnel. A mathematical model is depicted in Figure 1 below:

Figure 1. Self-correcting wind tunnel theory for two control surface static pressure.

Key: A--external field of flow boundary; B--foward field of flow boundary; C--aft field of flow boundary; D--region II; E--wind tunnel; F--second control surface; G--common region; H--first control surface; I--region I; J--main; K--wind tunnel axis; L--stream angle; M--main

By taking the first and second control surfaces as boundaries, the fields of flow are broken into regions I and II and a common region III or three components altogether. Region I plus the common region makes up the interior field of flow. Region II plus the common region makes up the exterior field of flow. In theory, region II should approach a boundaryless state. The first and second control surface's parameters of flow are separated into ϕ_{x1} and ϕ_{x2}. Lower coordinate regions E and T are separated to express an external field of flow and an internal field of flow. N is the iteration number for the self-correcting wind tunnel.

We start our calculations from the solution for the internal field of flow. The external boundary conditions for the initial field of flow are $\phi_{x2T}^{(0)} = 0$ which is for the boundary conditions at the mouth of the wind tunnel. In computations for the internal field of flow for the first control surface, the distribution of perturbation velocity for the x orientation is $\phi_{x1T}^{(N)}$ and this creates the internal boundary conditions for the external field of flow, so

$$\varphi_{x1E}^{(N)} = \varphi_{x1T}^{(N)}$$

In computations for the external field of flow for the second control surface, the distribution perturbation velocity for the x orientation is $\phi_{x2E}^{(N)}$. As an example

$$\varphi_{x2E}^{(N)} = \varphi_{x2T}^{(N)}$$

So we have $\varphi_{x2T}^{(N+1)} = K \varphi_{x2E}^{(N)} - (1-K)\varphi_{x2T}^{(N)}$

Consecutive calculations are made for the internal field of flow's external boundary conditions. Within the self-correcting wind tunnel, relaxation factor was preset to the value of K = 0.5 for purposes of this paper. For iteration, this factor led to a direct convergence.

The flow of calculation is depicted in Figure 2.

Figure 2. Flow of numeric simulation calculations for two surfaces self-correcting wind tunnel static pressure. Key: A—selected; B—(initial conditions); C—internal field of flow difference iteration calculations; D—external field of flow difference iteration calculations; E—calculation of airfoil surface pressure coefficient; F—true; G—false
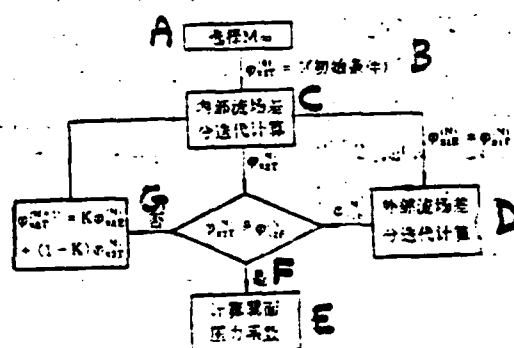
The boundary conditions for the internal field of flow are expressed below:

forward field of flow boundary $\phi = 0$

aft field of flow boundary $\phi_x = 0$

second control surface $\phi_{x2T}^{(0)} = 0$ (initial conditions)

$$\varphi_{i,j}^{(N)} = K\varphi_{i,j}^{(N)} - (1-K)\varphi_{i,j}^{(N)} \tag{2.1}$$

Wind tunnel axis line

air foil exterior $\phi_y = 0$

point on forward edge $\phi_x = -q_\infty$

top of airfoil when stream angle is at zero

$$\varphi_i = (q_x + \varphi_i)\frac{dy_i}{dx}.$$

The boundary conditions for the external field of flow are cited below:

forward field of flow boundary $\phi = 0$

aft field of flow boundary $\phi_x = 0$

upper field of flow boundary $\phi_y = 0$

first control surface $\phi_{x1E}^{(N)} = \phi_{x1T}^{(N)}$ $\qquad$ (2.2)

The aforementioned boundary conditions for (2.1) and (2.2) may be altered to take the form below:

The internal field of flow's x orientation mesh interval is Δx, so

$$\varphi_{i,j}^{(N+1)} = K\varphi_{i,j}^{(N)} + (1-K)\varphi_{i,j}^{(N)} \tag{2.1a}$$

and $\qquad \varphi_{i,j}^{(N)} = \varphi_{i,j}^{(N)}$ $\qquad$ (2.2a)

It is much more convenient to use (2.1a) and (2.2a) instead of (2.1) and (2.2.).

Calculation results are depicted in Figures 3-6. For the NACA 0012 airfoil, $M_\infty = 0.9$ and P=2 iteration method was used. For the RAE 104 airfoil, $M_\infty = 0.8$, and the P=1 iteration method was used. The internal field of flow and the external field of flow were separated for relaxation iteration. After two iteration trials, convergence on the objective occurred. The minimum absolute values for perturbation velocity potential of each node was 10^{-5}, and the maximum values were less than 10^{-3}. At this
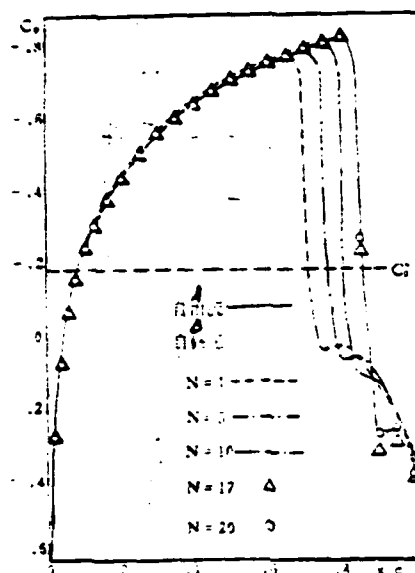
Figure 3. Airfoil pressure
distribution comparisons for
the NACA 0012 in free flow and
self-correcting wind tunnel.
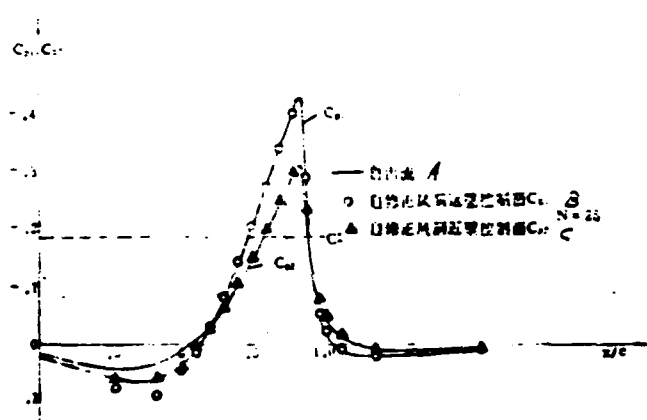
A--free flow; B--self-correction

Figure 4. Comparisons of control surface pressure
distribution for NACA 0012 airfoil, $M_\infty = 0.9$, $\alpha = 0^\circ$
in free flow and self-correcting wind tunnel.
A--free flow; B--self-correcting wind tunnel far wall control
surface; C--self-correcting wind tunnel near wall control
surface

point, after the separation convergence for the external field of
flow, we made a comparison of it with the nodal points of the
second control surface for perturbation velocity within the flow.
When the greatest absolute difference value obtained was 10^{-4}, it
was recognized as a convergence to no wind wall disturbance within
the self-correcting wind tunnel.

Calculation results for free flow and self-correcting wind
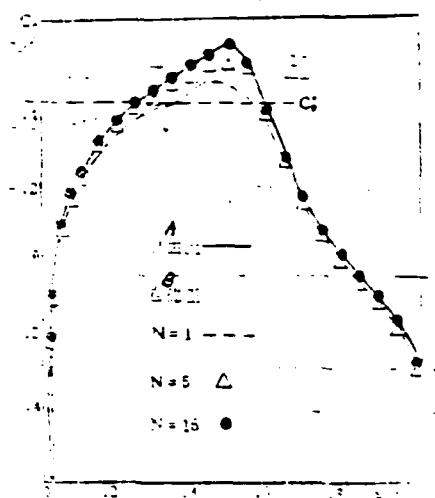tunnel static pressure distributions for both types of airfoils

Figure 5. RAE 104 airfoil pressure distributions in free flow and self-correcting wind tunnel ($M_\infty = 0.8$, $\alpha = 0°$).
A--free flow; B--self-correction

are depicted in Figures 3 and 5. The results obtained for both calculation methods are similar.

Calculation results for free flow and self-correcting wind tunnel pressure distributions for two control surfaces are compared in Figures 4 and 6. The results obtained for both of these methods is nearly identical.
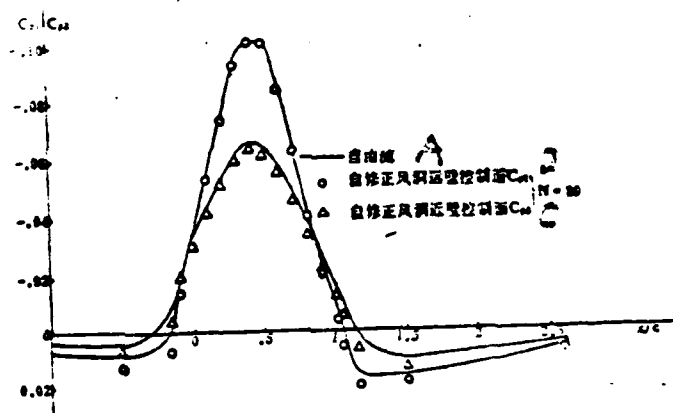

Figure 6. Comparisons of control surface pressure distributions for RAE 104, $M_\infty = 0.8$, $\alpha = 0°$, in free flow and self-correcting wind tunnel.
A--free flow; B--self-correcting wind tunnel far wall control surface; C--self-correcting wind tunnel near wall control surface

In consideration of measurement and discernment of two control surface static pressure distributions, there are certain difficulties. This article proposes a different scheme for self-correcting wind tunnels. A mathematical model is depicted in Figure 7.
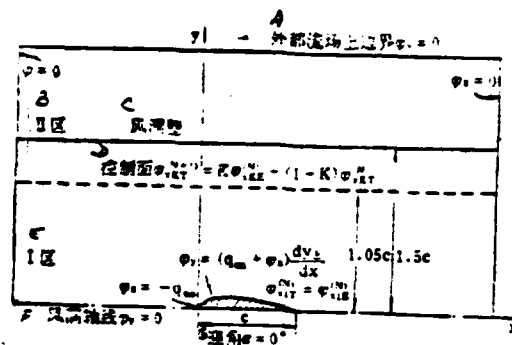
Figure 7. Principles of self-correcting wind tunnel as applied to control surface and airfoil static pressure.
A--upper boundary of external field of flow; B--region II; C--tunnel wall; D--control surface; E--region I; F--wind tunnel axis; G--stream angle
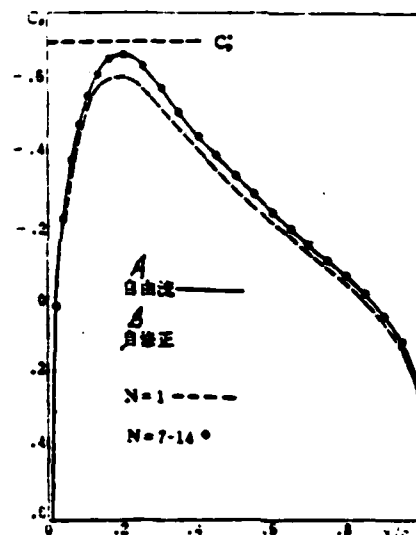

Figure 8. Comparison of airfoil pressure distributions in free flow and self-correcting wind tunnel for NACA 0012, M_∞ = 0.72, $\alpha = 0°$.
A--free flow; B--self-correction

By taking the control surface as a boundary, we can separate the field of flow into two components, region I and region II. Region I is the internal field of flow. Region I plus region II comprise the external field of flow. In theory, region II nears an unlimited or unbounded state. The atmospheric flow parameters for the control surface and the airfoil are divided into φ_{eK} and φ_{si} . Lower boundaries E and T express external flow and internal flow fields. N is the self-correcting wind tunnel iteration number.

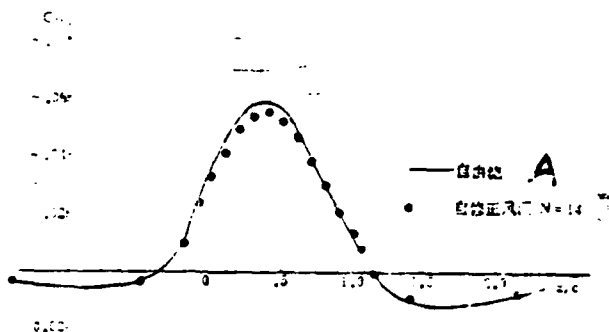Figure 9. Comparison of air
foil pressure distributions
in free flow and self-correct-
ing wind tunnel for NACA 0012,
$M_\infty = 0.72$, $\alpha = 0°$.
A--free flow;
B--self-correcting wind tunnel

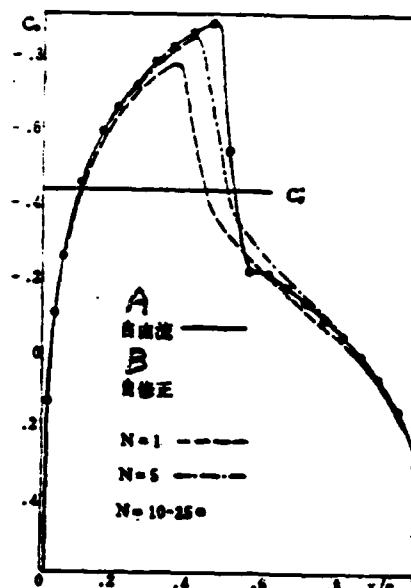Figure 10. Comparison of
airfoil pressure distributions
in free flow and self-correct-
ing wind tunnel for NACA 0012,
$M_\infty = 0.8$, $\alpha = 0°$.
A--free flow
B--self-correction

Starting with calculation of a solution for the internal
field of flow, the initial internal field of flow's external
boundary conditions are $\phi_{xKT}^{(0)} = 0$. From the internal field of
flow, we calculate the x orientation perturbation velocity dis-
tributions for the airfoil as $\phi_{x1T}^{(N)}$. By using $\phi_{x1T}^{(N)}$ as the internal
boundary conditions for the external field of flow, we have

$$\varphi_{x1E}^{(N)} = \varphi_{x1T}^{(N)}$$

From within the external field of flow, we can calculate the con-
trol surface's x orientation perturbation velocity distribution
$\phi_{xKE}^{(N)}$.

For example
$$\varphi_{xKE}^{(N)} \neq \varphi_{xKT}^{(N)}$$

which yields
$$\varphi_{xKT}^{(N+1)} = K\varphi_{xKE}^{(N)} + (1-K)\varphi_{xKT}^{(N)}$$

which becomes the internal field of flow's external boundary
conditions on successive calculations. Herein, K is the relaxa-
tion factor for the self-correcting wind tunnel. This article
set the value of $K = 0.5$. For iteration, it led to a direct
convergence. The calculation model is depicted in Figure 2.

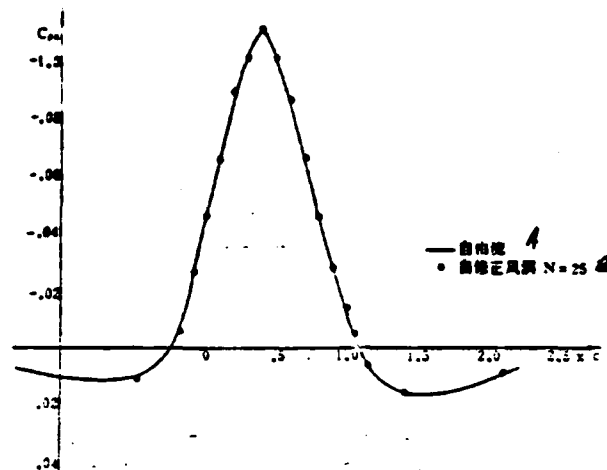The internal field of flow boundary conditions is expressed
below:

Figure 11. Comparisons of control surface pressure
distributions in free flow and self-correcting wind
tunnel for NACA 0012 airfoil, $M_\infty = 0.8$, $\alpha = 0°$.
A--free flow; B--self-correcting wind tunnel

forward field of flow boundary $\phi = 0$

aft field of flow boundary $\phi_x = 0$

control surface $\phi_{xKT}^{(0)} = 0$ (initial conditions

$$\varphi_{xKT}^{(0)} = 0 (初始条件)$$

Wind tunnel axis $\varphi_{xKT}^{(N+1)} = K\varphi_{xKE}^{(N)} + (1-K)\varphi_{xKT}^{(N)}$

    airfoil exterior $\phi_y = 0$

    point along forward edge $\phi_x = -q_\infty$

    top of airfoil, as stream angle is zero

$$\varphi_y = (q_x - \varphi_x)\frac{dy}{dx}$$

External field of flow boundary conditions is shown below:

    forward field of flow boundary $\phi = 0$

    aft field of flow boundary $\phi_x = 0$

    upper field of flow boundary $\phi_y = 0$

Wind tunnel axis

    airfoil exterior $\phi = 0$

    point along forward edge $\phi = -q_\infty$

    top of airfoil $\phi_{x1E}^{(N)} = \phi_{x1T}^{(N)}$

Calculation results are shown in Figures 8-11. The P=2
iteration method was used. The convergence for internal and
external flow relaxation iteration and the convergence for the

self-correcting wind tunnel is in Section 2. For the NACA 0012 airfoil, M_∞ = 0.72, 0.8, α = $0°$. Both calculations for free flow and self-correcting wind tunnel are compared in Figures 8 and 10.

For both computations, the results are similar. Both calculations for control surface pressure distributions in free flow and self-correcting wind tunnel are compared in Figures 9 and 11. The results for both calculation methods are nearly identical.

IV. Conclusion

Based on numeric experimentation, the findings of this document show improved stability characteristics for the longitudinal large perturbation and transverse small perturbation transonic flow around a symmetric airfoil in a zero stream angle and in linear relaxation where the difference formula for ϕ_{xx} uses improved iteration and the difference formulas for ϕ_x uses a simple iteration.

In regards to transonic velocity zero lift symmetric airfoils and self-correcting wind tunnels, this document proposes using the self-correcting method for static pressure for a two-control surface airfoil and the self-correcting method for static pressure on a one-control surface airfoil. In this way, numeric simulation can prove a convergence.

The research of this document can be generalized to tri-elemental flow in a non-zero lift state.

REFERENCES

[1] Liu Xueding. Research on wind tunnel wall vibration and transonic velocity airfoils, Northwestern Polytechnical University, Graduate Thesis, February 1983.

[2] Xuan Youwen, Luo Shijun. A discussion of convergence and stability characteristics for potential flow line relaxation for normal transonic velocity small perturbation surfaces, Journal of Aerodynamics, 2 (1983), 20-28.

[3] Wang Shumo. Self-correcting wind tunnel convergence for zero lift airfoils at transonic velocity, Journal of Aviation, 1 (1980), 8-11.

[4] Luo Shijun, et al. Transonic velocity potential flow mixed difference methodology, National Industrial Publishing Society (1979).

ON RELAXATION OF TRANSONIC FLOWS AROUND ZERO-LIFT AIRFOIL AND CONVERGENCE OF SELF-CORRECTING WIND TUNNELS

Liu Xueding, Luo Shijun

(Northwestern Polytechnical University)

Abstract

With the assumption of small transverse velocity components, the steady transonic potential flow around symmetric airfoil at zero angle of attack is computed by the mixed difference method. After some numerical experiments on the stability of various possible schemes of iteration in the relaxation, a stable scheme is found and used to verify the convergence of two kinds of transonic self-correcting wind tunnels which are based on the pressure distributions along (1) two control surfaces and (2) one control surface and the airfoil.

OBSERVATION OF FLOW DIAGRAMS FOR EXPANSION SHOCKWAVE TUBE

Yu Hongru, Lin Jianmin, Li Zhongfa and Gu Jiahua

1. FOREWORD

The calculation methodology for uniform shockwave tubes has
already developed to near perfection. In order to obtain an intense
shockwave, we often make use of a "contracting" shockwave tube.
Its booster section is about the same as a booster stage. A diaph-
ragm has been added to allow the nozzle to contract. A large
booster stage is only required in research on low density gases
or in low intensity shockwave research. In order to reduce the
quantity of gas used in the booster, the "expansion" shockwave
tube is generally selected for utilization. Its booster section
is smaller than a booster stage, and expansion through the nozzle
is similar for both types. In regard to the shockwave tube move-
ment at the slotted boundary region, a contraction-expansion
nozzle is often placed in the lower portion of the diaphragm to
prevent the mutual interference from the rarefaction wave and the
reflex shockwave from occurring or it is done in order to obtain
a polar extreme shockwave. As for this type of variational sec-
tional shockwave tube flow, Resler, et al. [1] states that for the
contracting shockwave tube, it becomes a matter of sonic or super-
sonic flow as it passes through the lower nozzle area, and he pro-
vided a calculation methodology for shockwave intensity. Alpher
and White [2] took the methodology provided in bibliographical
reference [1] and added to it, making several improvements. They
advocate use of a diaphragm with a nozzle that can be adjusted for
various types of flow, and not only can the nozzle be set for
sonic or supersonic flow, but furthermore, the nozzle can be set
for subsonic flow as well.

If the transition nozzle is of the expansion type, Roscizewcki
[3] points out: when the nozzle is at supersonic flow, it exists
in two different and distinct types of flow wave diagrams--as pre-
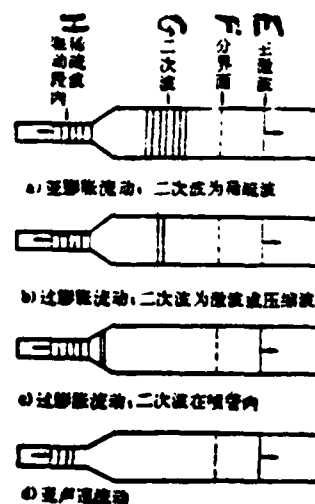expansion in the lower reaches manifests itself as a rarefaction

wave, and as post expansion manifests itself as a secondary shock-
wave. The two aforementioned theories are both based on regulated
flow of the booster gases. This is because it is not suitable to
use with the secondary shockwave flow that ensues. Laderman [4]
provides a method of flow calculation for the secondary shockwave
that comes about.

Russel [5] makes a diagnosis for expansion shockwave tube flow.
The theory for conditions of pre-expansion predicts that the rare-
faction wave in the lower reaches of the nozzle will be very easily
observed. However, the theory for conditions of post expansion
secondary shockwaves in the lower reaches of the nozzle were not
observed as predicted.

The contents of this document show successive experimental
observation results for expansion shockwave tube flow as well as
the corresponding flow diagrams for actual conditions of flow as
they exist.

Figure 1. Four types of wave
flow systems for shockwave
tubes
a--pre-expansion flow, secondary
shockwave as rarefaction wave;
b--post-expansion flow, secondary
wave as shock or compression wave;
c--post-expansion flow, secondary
wave in nozzle interior; d--sub-
sonic velocity flow; e--primary
wave; f--boundary region; g--sec-
ondary wave; h--rarefaction wave
at booster interior

2. DIAGNOSTIC METHOD

The expansion shockwave tube exists in four different forms
of flow conditions (Figure 1).

a. When the primary shockwave and the Mach number exceed a
specified critical value, a rarefaction wave manifests in the lower
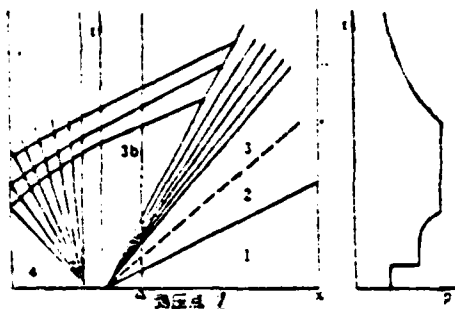reaches of the nozzle. This particular type of flow is referred

43

Figure 2. Pre-expansion
wave diagram and curvi-
linear pressure data.
1--measured pressure
points

图2 正逆流变图及压力曲线形状

Figure 4. Recorded curvi-
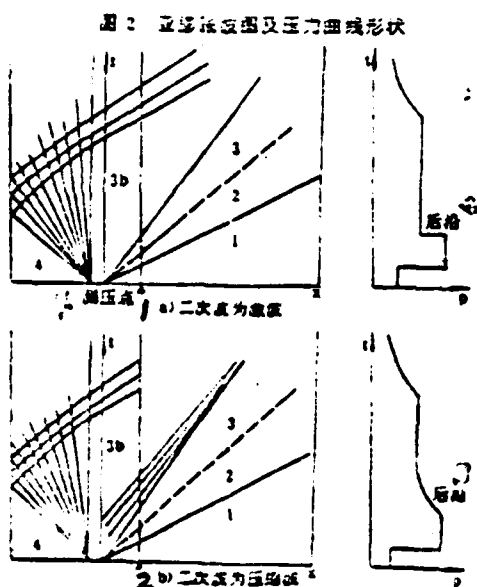linear pressure data for
differing Mach numbers.

Figure 3. Post-expansion
wave diagram and curvi-
linear pressure data.
1--secondary shockwave as
compression wave; 2--secondary
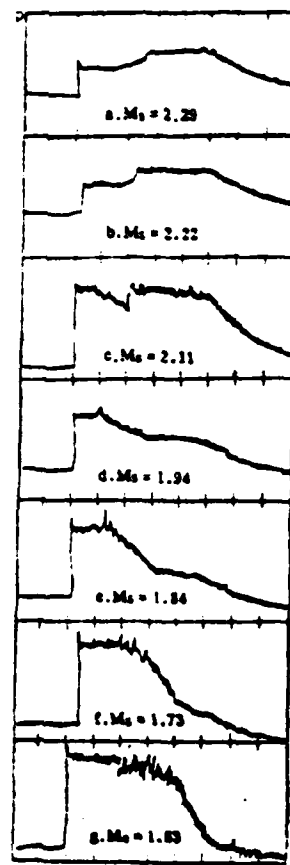wave as shockwave; 3--rear edge;
4--measured pressure points

This document was received on March 12, 1984

44

to as pre-expansion flow. If a pressure blockage occurs within
the lower reaches of the nozzle tube, the pressure curvilinear
conditions and formulas are as expressed in Figure 2. Following
a decrease in the intensity of the primary shockwave, the rare-
faction wave begins its decay process. At the time when the
rarefaction wave has equalized to that of the Mach wave, we refer
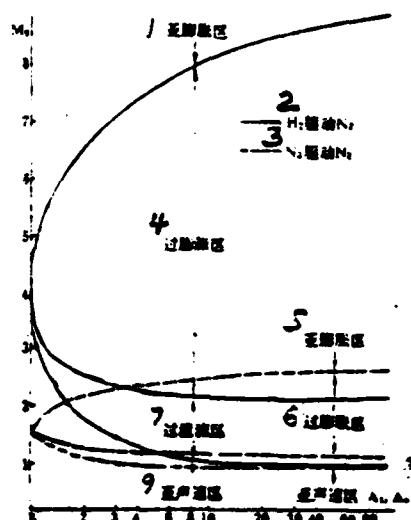to this moment as the "greatest disturbance" of expansion.

Figure 5.   Realm of four
types of expansion shock
wave tube flow fields.
1--pre-expansion region;
2--H N propellant;
3--N N propellant;
4--post-expansion region;
5--pre-expansion region;
6--post-expansion region;
7--post-expansion region;
8--subsonic area;
9--subsonic region

b.   When the primary shockwave
and the Mach wave decrease to "greatest
disturbance", the primary shockwave
transitions to a post expansion flow.
If Rosczizewcki foresaw that particular
type of manifestation occurring as a
secondary shockwave, the pressure curve
conditions and corresponding wave flow
diagrams would be as depicted in Figure
3a.   Due to the disturbance that exists
within the boundary layer of actual
flow, it is clear that it can only
exist as a compression shockwave. At
this time, the curve measurements for
pressure conditions and the correspond-
ing wave flow diagrams would be as are
shown in Figure 3b.

c.   As the intensity of the primary shockwave successively
decreases, the secondary shockwave or compression wave moves into
the interior of the nozzle.

d.   With a further decrease in the intensity of the primary
shockwave, the booster gases change completely and become subsonic
flow.

The contraction shockwave can, therefore, only exist under
flow conditions a and b.

This experiment is limited to observation of the two types of flow depicted in wave diagrams a and b. From a comparison of Figures 2 and 3, we can see the following: A differentiation of pre-expansion flow and post-expansion flow based on whether or not the aft platform is positioned higher than the forward platform (mounting platform). The result of a post-expansion flow is a secondary wave or a compression wave which is reliant upon the existing pressure curve conditions. If we can overlook the influences of the boundary layer and the sensing devices, the secondary shock wave has a steep trailing edge; furthermore, the trailing edge of the compression wave that is produced has a definite, specific width. In actual measurements, there was a specific dimension given for the sensing devices, and the secondary shockwave passed through the sensing device using up a specified amount of time. This, coupled with the primary shockwave that previously occurred, creates our boundary layer. As this fork or division occurs, a certain amount of time is required for it to pass through the sensing devices. As a result, there is a gap of a specific width in the measurements taken for the pressure curve. However, for a comprehensive analysis, the two widths cannot be the same. We must base our diagnosis on the dimensions of one of these widths.

3. EXPERIMENTAL RESULTS AND DISCUSSION

An expansion shockwave tube was used for all of the experiments cited in this document. The booster section had an interior diameter of 80 mm, it was 2000 mm long; the passive booster stage had an interior diameter of 185 mm, and it was 5000 mm long. They both used the same type of shockwave tube diaphragm. The operational fuel used for the booster section and the passive booster was ambient nitrogen. Attached to the nozzle port was a 1.22 m slotted piezo-electric sensing device, used to record the pressure over time curve data, as outlined in Figure 4. From an analysis of the curve data in the fiture, we can make the following assumptions:

46

(1)   Figures 4a and 4b are split into $M_s = 2.29$ and $M_s = 2.22$ for the pressure curves. Since the forward platform is lower than the lower platform $(p_2 < p_{3b})$, we can diagnose this as pre-expansion flow.

(2)   Figure 4c is for the pressure cufves at $M_s = 2.11$. The forward and aft platforms are nearly equal ($p_i \approx p_{ib}$), so we can recognize this as a condition of near "greatest disturbance" for the compression. The following data is revealed from the convex curvature that manifests: under those conditions of near "greatest disturbance" in compression, the upper reaches of the boundary layer did not smooth out as theoretical predictions had expected. Further-more, there was a turbulence present which can only lead us to conclude that it was a result of mutual interference.

(3)   Figures 4d, e and f are split into curves for $M_s = 1.94$, $M_s = 1.84$ and $M_s = 1.73$. The forward platform was higher than the aft platform $(p_2 < p_{3b})$ indicating a post compression flow. The time required to pass through both platforms was about 3 ms. The velocity of the primary shockwave was approximately 6×10^2 m/s. The primary shockwave required approximately 2-3 ms to reach its peak, and the secondary shockwave required about 2-4 ms. The velocity of the secondary shockwave was 10^2 m/s. If we consider the secondary shockwave as a primary wave of ± 5.5 mm, the time required for it to pass through the sensing devices would be about 10^{-2} ms; the primary shockwave passed through the boundary conditions and a division was formed that is demarcated with the wide-line recordings. The time required for the primary shockwave to pass through the sensing devices was approximately 10^{-1} ms. For all three of the above con-ditions, the elapsed times were about 3 ms. From this, we can assume the secondary shockwave to be a compression wave.

(4)   Figure 4g is for the curve of $M_s = 1.63$. The aft platform for this condition was not clearly measured, so the pressure booster stage reaction was inconclusive.

The results of the above observations and analyses can be summarized as follows: $M_s > 2.11$ is a condition of pre-expansion. The boundary layer itself is actually a part of the rarefaction wave. $M_s < 2.11$ is a condition of post-expansion. The boundary layer here exists as a part of the secondary shockwave, as was predicted in bibliographical reference [3]. Actual observations support this assertion.

The expansion shockwave tube flow fields exist in four different forms. In analysis and calculation, we must recognize which of these conditions is affecting the flow under study, and then make the proper choice as to which calculation methodology is best suited for use. Figure 5 depicts the realms of each of the four types (limited to our study, aside from the calculation formulas). From the figure, we can see: post-expansion flow occupies a specified width within its realm. Many of the actual parameters used are derived from this region. If post-expansion exists in the secondary shockwave, then its calculation method will be different from that for pre-expansion. If the post-expansion exists as a compression wave, then the rarefaction wave is produced in the pre-expansion area in abnormal fashion. Parameters used for fore and aft wave systems are similar. Because the post-expansion area can be substituted in the formula for pre-expansion, the resultsd are found in a very convenient manner.

I would like to thank Comrades Gu Shengxue and Li Zhenhua for their help in taking measurements during this experiment.

E c contact of References.

[1] Resler, E. L., Lin, S. C. & Kontrowitz, A. Jour. Appl. phys.,Vol 23, 1952, p.1390.
[2] Alpher. R. A. & white, D. R., Jour. Fluid Mech.,Vol 3, part 2, 1958.
[3] Rosciszewcki, J., Phys. Fluids, Vol 5 , No 1, 1962.
[4] Lederman, A. L., AIAA Jour., Vol 5, No 10, 1967.
[5] Russell, D. A., Phys. Fluids, Vol 5, No 4, 1962.

OBSERVATION OF WAVE DIAGRAMS FOR SHOCK
TUBE WITH THE DIVERGENT NOZZLE AT
DIAPHRAGM SECTION

Yu Hongru, Lin Jianmin, Li Zhongfa, Gu Jiahua

(Institute of Mechanics, Academia sinica)

Abstract

Piezoelectric pressure data were obtained in ϕ 185mm shock tube with divergent section at shock Mach number range $1.5 < M_s < 2.5$. It is shown that in underexpansion flow exist rarefaction wave as previous predict, but in overexpansion flow exist compressive waves instead of secondary shock wave which was predicted by Roscizewcki[3].

A NUMERIC CALCULATION METHODOLOGY FOR THE INFLUENCES
OF GROUND TO AIR INTERFERENCE

Chen Zhengcai

(Chinese Aerodynamic Research and Development Center)

1. FOREWORD

Take-off and landings are important stages of flight for an aircraft. When an aircraft is flying very close to the ground, it can be influenced by the effects of ground to air turbulence, and this is called the "ground effect". Generally speaking, it causes the aircraft lift to increase. Normally, the angle of attack for take-off and landings is a = 8-12°, and for some foreign aircraft, it may be as high as approximately 20°. With wing flap deflection angle δ = 25°-45°, the ground effect can be quite serious, even to the point of producing obviously non-linear effects. The longitudinal moment of force and the trim can both produce very obvious changes. As a result, when designing new aircraft, the topic of ground effect has become an absolute necessity for inclusion in the research.

To determine the unique ground-atmospheric influences on new aircraft, what is most often used is a fabricated experimental floor model for use in a low velocity wind tunnel. A level flow stream across the floor is used to simulate the ground. The floorboards are usually permanently attached in the wind tunnel. Clearly, this cannot actually simulate the true conditions because in true flight conditions, the aircraft is what is really moving. The ground does not move relative to the atmosphere. Nevertheless, in testing, the floor plates and the atmosphere are what is moved. This reveals the reasoning for an attached surface layer existing on the floor. This can be overcome by using the atmospheric wind tunnel flow velocity to account for floor motion. However, because of the structure and other factors, it is not really adequate.

After using lift linearization and precision lift plane (sectional) theories to calculate the wing's ground effect, the results proved to have relatively large error differences, even so much so as to possibly directly oppose the experimental outcomes. Later, after pouring over the calculation methodology for the ground effect in lift plane theory, we saw that there was no calculation results applicable to the aircraft as a whole. Therefore, in research on the problems of ground effect, this has generated a great deal of concern.

In the studies of aerodynamic calculations, bibliographical reference [1] provides an introduction to the methodlogy, and from it we can extend these learnings to a vast range of applications, such as to the validity of complicated calculations or even to simpler methodologies. This document uses some of those methods to calculate the ground effect for the wing and the entire aircraft. In calculation, the planar surface and tail profile are both considered as being non-linear, the flaps and the fuselage are considered deflectors. This allows the results of calculation to be sufficiently accurate.

2. CALCULATION METHODOLOGY

For the problem of ground effect, a solution for air flow pressure can be found in the equation:

$$\frac{\partial^2 \varphi}{\partial x^2} + \frac{\partial^2 \varphi}{\partial y^2} + \frac{\partial^2 \varphi}{\partial z^2} = 0 \tag{1}$$

In the equation, x, y and z are the three coordinate axes within the coordinate system. φ is the interference velocity potential. To satisfy all of the boundary conditions, we include the following: influx flow non-interference and wing surface's rear edge Kutta conditions as well as the planar surface and ground interference flow stream conditions. The problems associated with these unique conditions, in comparison with the calculations for normal flight aerodynamics, are that we cannot bypass the ground flow conditions. Because of the limitations of the ground surface, we handled this as an infinitely large "mirrored surface". By using the mirror

surface profile, we are able to satisfy the special conditions for this problem.

This document separates the aircraft calculations into segments for the wing system (wing and elevators) and the rotation around the body's planar surface. A finite element, fundamental solution problem solving method is used for the equations. At the same time, the fundamental solution figures for a calculation model of the aircraft's profile are given below:
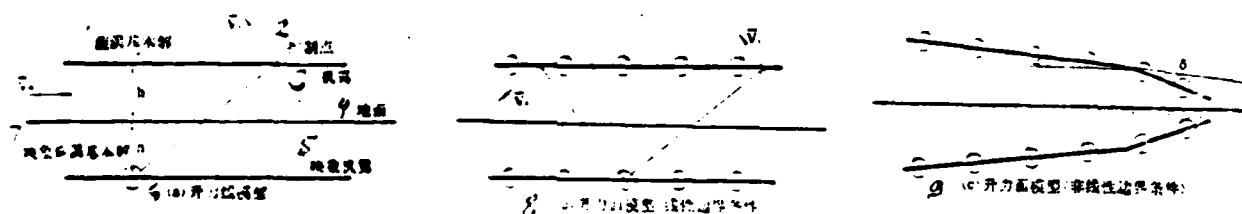
Figure 1 Several models of aircraft wing ground effect calculations.
1--fundamental solution of vortex; 2--control point; 3--aircraft (illeg.); 4--ground; 5--image of wing; 6--(a) linear lift model; 7--fundamental solution of vortex image; 8--(b): lift model linear boundary conditions); 9--(c): lift model (non-linear boundary conditions)

WING. The aircraft wing is, along its level surface area, sectioned off into trapezoidal grids. Distributed at each mesh point in the grid is a fundamental Kutta solution for the successive U-shaped vortex intensities and the consecutively stronger vortex intensities which are similar. The image of the fundamental solution intensity is generally the same as the wing image's fundamental solution. Only the axis of the vortex will differ (see Figure 1). The boundary condition control point is established from the center of the grid. Thus, the problem can be solved in the matrix equation below:

$$[A - \bar{A}]\{\Gamma\} = -\{V_n\}$$

(2)

In the equation, A ($\bar{A}$) is the wing's fundamental solution (maged fundamental solution) coefficient of influence. Γ is the fundamental solution for intensity. V_n is the planar orientation velocity.
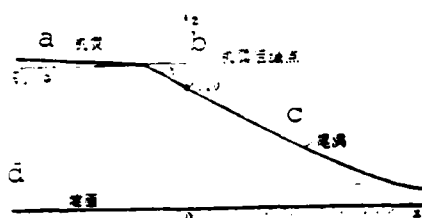
52

Figure 2. Tail vortex coordinate system wing a--wing; b--point in rear edge of wing; c--tail vortex; d--ground

Figure 3. Quantitative lift for two-dimensional wing ground effect.
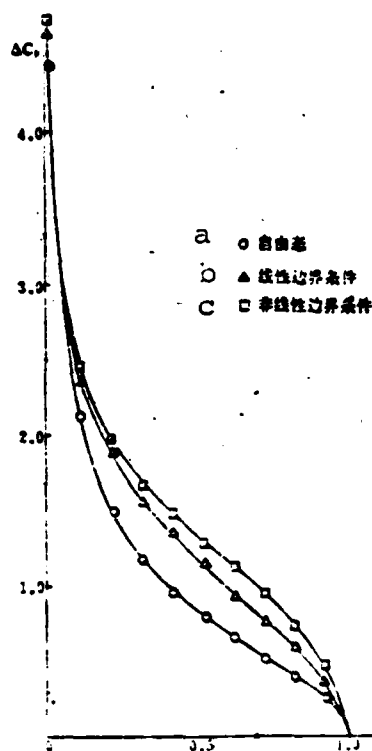a--non-linear conditions;
b--linear conditions

Figure 4. Two-dimensional wing with and without ground interference load distributions.
a--free form; b--linear boundary conditions;
c--non-linear boundary conditions

Figure 5. Two-dimensional wing ground effect lift coefficents which follow changes in ground to air distances.
a--linear boundary conditions;
b--non-linear boundary conditions
c--free form accuracy figures

We are obliged to point out the following: the problem with the ground effect calculations using linear boundary conditions is that the calculation error can be fairly large. This document uses non-linear boundary conditions (see Figure 1). At the same time, the U-shaped vortex of the tail eddy at the rear edges of the wing are dragged through the boundary. Furthermore, for the unlimited planar surface at the aft section, there is a gradual linearization to ground. An equation for the principles of the tail vortex (Figure 2) is:
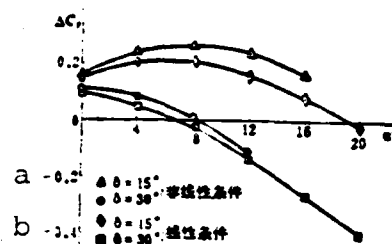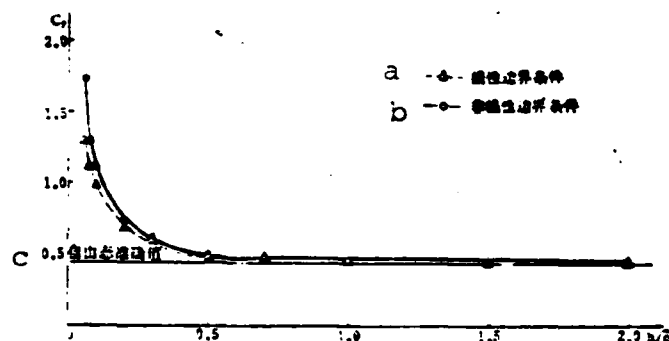
$$z = \left(\frac{1}{c^{\prime\prime\prime\prime\prime}} \right)^{\prime}$$

(3)

BODY. Suppose within a body of revolution, the axis line is divided into a dispersion source and a vortex origin, wherein the fundamental solution can substitute for the interference field. The source lies within the grid's center; the vortex origin lies at the head of the grid. Opposite the ground, there is no change in the source image and the intensity of the vortex origin is equivalent, but it lies opposite the axis line. The boundary condition points are taken in a source location that is opposite the planar surface, either upper or lower profile. The matrix solution can be found in the equation:

$$[B - \bar{B} - G - \bar{G}]\{Q - R\} = -\{I^{\prime}\}$$

(4)

In the equation, B and G express dispersion and vortex source influence coefficients. Q and R differentiate between their respective intensities. "1" expresses the image quantity.

3. CALCULATION RESULTS

Calculation results for the aircraft components and the aircraft as a whole, as mentioned above, are given below.

TWO DIMENSIONAL WINGS

This document uses an aspect ratio of $\lambda = 80$ for the rectangular wing and the chord orientation, which is separated into two sections for two dimensional results. This seems to be the most rational methodology.

Ground effect generally causes conventional changes that increase aircraft wing lift. The reasons for this are shown in Figure 1(a) which illustrates the linear lift theory. However, the fact of the matter is that there are times when lift may actually be reduced (see Figure 3). Figure 1(b) illustrates a model that considers the chord angle to load distribution. The rationale here is that of Figure 1(c) which illustrates a model with non-linear boundary conditions. This is the calculation methodology that is used in this document.

54

Figure 4 shows chord orientation to load distribution, and
Figure 5 illustrates when a = 4° lift coefficient, which follows
the curvilinear changes in distance and altitude h. As one can
see, the linear boundary conditions and non-linear boundary condi-
tions have large differences in their calculation results. When
the distance between ground and altitude is equal to one times the
chord length value, the ground effect has already become very
feeble. Lift is increased approximately 5% and at a point which is
two times the chord length value, it is minimal and may even be
neglected since it is not worth the trouble of calculating. However,
when it is lowered to 0.5 times the chord length, it is very clearly
seen and lift shows a quantitative increase of as much as 15%.

THREE DIMENSIONAL WINGS

Figure 6 and Figure 7 are for λ = 2.8 for a rectangular wing's
lift and moment of force calculation results [2]. At the same time,
they provide test values and results from international experiments
which can be used to make quantitative comparisons with our results
to adequately satisfy our needs. Moreover, the ground effect
causes the linear lift slope to increase = $0.2\bar{c}$ ($\bar{c}$ is the average
aerodynamic chord length) when it is greater than 90%. When h =
$1.0\bar{c}$, within 10% approximately, we can see the three dimensional
wing ground effect is a much more severe problem than when compared
to ground effect for a two dimensional wing. This is because of
the greater image interference of the tail vortices system.

ENTIRE AIRCRAFT

The calculations for the entire aircraft were done as outlined
in bibliographical reference [3] of this document. The model for
the body was a 12 scale replica tapered body. The wing was tri-
angular, λ = 3.0. The tail was waist tapered, λ = 4.0 (Figure 8).

Figure 9 depicts a curve of the entire aircraft's moment of
force characteristics. The test values of the figure were pro-
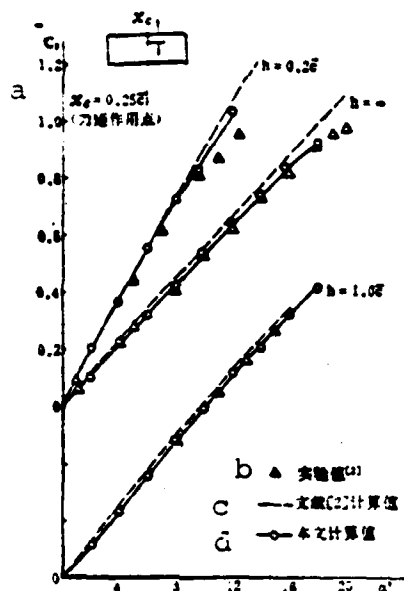vided from bibliographical reference [3] which were taken from the

Figure 6. Rectangular wing
(λ=2.8) with and without
ground interference lift
characteristics.
a--point used for moment of
force; b--test figures; c--
calculation figures of biblio-
graphical reference [2]; d--
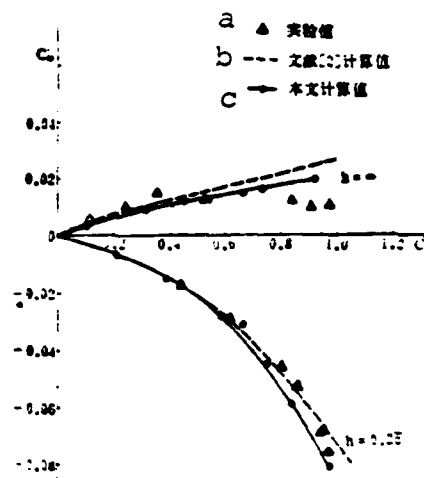calculation figures of this
document

Figure 7. Rectangular wing
(λ=2.8) with and without
ground interference moment
of force characteristics.
a--test figures; b--calculation
figures of bibliographical
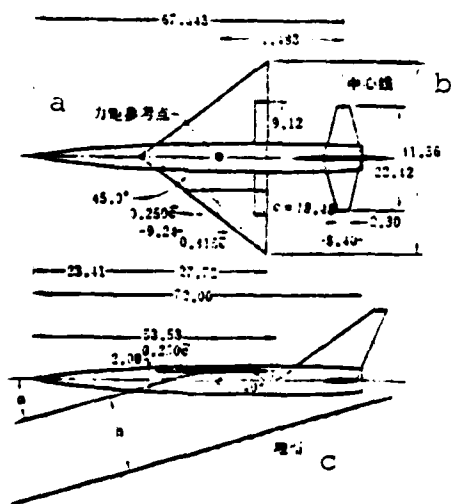reference [2]; c--calculation
figures from this document

Figure 8. Calculation model
for the entire aircraft.
a--consideration point for
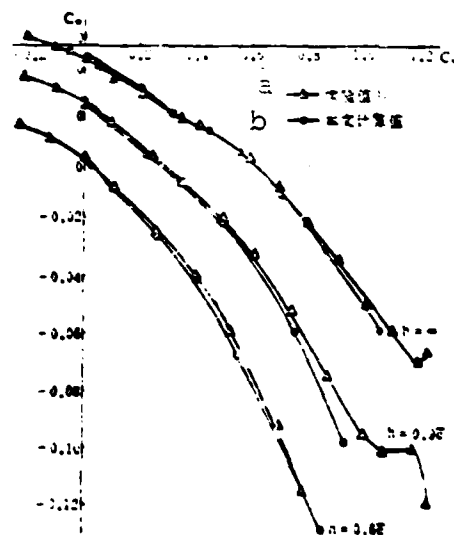moment of force; b--center
line; c--ground

Figure 9. Entire aircraft with
and without ground interference
moment of force characteristics.
a--test figures (3); b--calculation
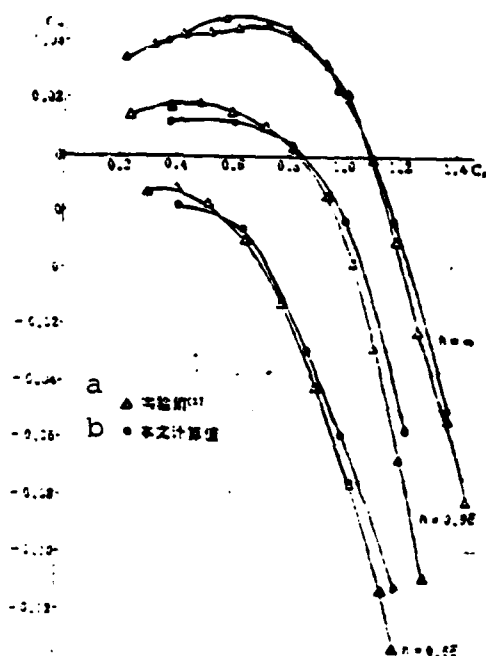figures of this document

56

Figure 10. Entire aircraft
(δ=40°) with and without
ground interference moment
of force characteristics.
a--test figures; b--calcul-
ation results of this
document

wind tunnel floor test results. The tail was stabilized with a deflection of 0.2°, which was the same as for the other tests. Regardless of the presence of ground interference, the calculation values and the experimental values both coincided quite nicely.

Figure 10, when the wing flap deflection is δ = 40°, shows moment of force curves for the whole aircraft. Although there is a large flap deflection, it is due to the non-linear boundary conditions which are used in this document, and the calculated figures coincide closely to other [3] test results.

The interference between the ground surface and the aircraft obviously changes with the moment of force curvilinear slope, and it influences the trim characteristics as well.

4. MAJOR CONCLUSIONS

1. For aircraft very close to the ground, when using a linear boundary condition to calculate all of the results for ground effect, the error difference can be very large. We must utilize non-linear boundary conditions that will allow us to account for conditions of deflection.

2. Analysis in basic linear lift theory allows us to obtain ground effect which, in general, causes aircraft wing lift to increase. Because the flaps have specific deflections at different altitudes, ground interference can actually cause a decrease in

57

lift. Linear lift theory does not account for these conditions.

3. The ground to aircraft flight aerodynamics are severely influenced by ground turbulence, and ground turbulence clearly alters the lift-line slope and in-flight aerodynamics.

4. The finite element fundamental solution calculation methodology is used to calculate flight ground effect and is a very effective method.

MAJOR CONTRIBUTING REFERENCES

[1] An Lianguang, Aerodynamic Research and Development, 1, (1978).

[2] Hummel, D., ZFW, 21, 12(1973).

[3   Buell, D. A., Tinling, B. E., NACA TN 4044.

A CALCULATION METHOD OF GROUND EFFECTS
FOR THE AIRCRAFT

Chen Zhengcai

(China Aerodynamic Research and Development Centre)

Abstract

When an aircraft is flying near the ground, it's aerodynamic characteristics may be influenced by the ground. Using the finite element solution method and the linear and nolinear boundary conditions, this paper gives a calculation method for the ground effects. Here the ground is considered as an infinite image plane and both the flap and the elevator can deflect too.

The calculation results for two-or three-dimensional wing and the wing-body-tail combinations are presented and these results are in a good agreement with the experiment data or other theoretical results. The calculation results for deflecting control surfaces are only given by our method.

The calculation results proved that using the linear boundary condition and the lifting line theory may sometimes produce the wrong results. especially as the wing is guite near the ground. By means of the nolin ear boundary condition and the lifting surface theory this method can get good results.

ON DETACHED SHOCK WAVES OF SPHERICAL BODIES AT
TRANSONIC VELOCITIES

Zheng Zhichu
(Institute of Mechanics, Academia Sinica)

1. FOREWORD

In recent times, the primary orientation of research for thick
bodied transonic linear flow has been within the realm of $M_\infty \approx 1$.
Within the range of $0.95 < M_\infty < 1.05$, especially for the area closest
to $M_\infty \approx 1$, results of theoretical calculation, experimentation and
wind tunnel tests for spherical bodies have provided evidence that
there are a great many differences which exist across a wide range
of detached spherical bodies. For an accurate measurement of the
shock waves and certain changes they undergo as the Mach number
changes, there is still no prescribed best method.

The calculations referred to in bibliographical reference [1]
point out the following: within the vicinity of $M_\infty \approx 1$, the changes
of the detached shock wave as it follows the changes in the M_∞
values are even more sensitive when compared to the physical plane
surface pressure distributions. As a result of this, at transonic
velocities, it is more accurate to use the spherical body detached
shock wave measurements as the Mach number changes instead of
using the pressure coordinates.

Based on the methods outlined in bibliographical reference [2],
we need only follow the rules outlined for detached shock waves
which follow M_∞ value changes within the vicinity of $M_\infty \approx 1$. We
can use a small arms ballistic range and common precision instru-
ments for measurement to obtain a resistance coefficient for the

---

spherical body at the vicinity of M_∞ . Afterwards, following a
comparison with generalized wind tunnel results, free-flight data
or magnetic suspension modeled wind tunnel results, we can research
the influence of the tunnel wall and center of resistance in regard
to spherical body aerodynamic coefficients [3].

In consideration of the aforementioned, it is of great signi-
ficance to note that all of the data provided within the realm of
transonic velocities when compared to the data for the region of
$M \sim 1$, runs counter to the simple equation for detached shock waves
of spherical bodies.

Since there is no center of resistance interference present in
a ballistics test range, it is comparable to a modern transonic
velocity wind tunnel. The ballistics test results are quite similar
to flight results in comparison [4]. This document uses the results
of ballistics range experiments as a foundation, then a comprehen-
sive analysis is done to determine the influence of each variable
on shock wave form with, for instance, the rules for the detached
distance δ, the shock wave slope tgβ, and the shock wave post-sonic
velocity position $\theta*$, etc., which follow the changes in the Mach
number M_∞. Furthermore, with all of the assimilated data results for
experiments conducted in recent history, using those values in the
range of $1 < M_\infty < 2$, a comparison of actual flow for spherical
detached shock waves of various forms can be used to create a simple
equation.

2. DETACHED SHOCK WAVE FORMULA

Spheres take the form of symmetrical axis bodies. Research
of spherical detached shock wave forms only requires consideration
of the meridian plane (see Figure 1). We all know that: when
$M_\infty \to \infty$, the physical body of the circular arc of the detached shock
wave is stationed directly in front of the sphere; moreover, in
the range $1 < M_\infty < \infty$ when it is within the region of $M_\infty \to 1$, the
spherical detached shock wave should follow the M_∞ values according
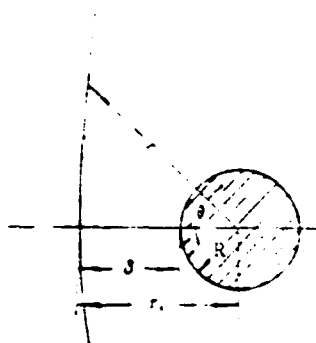
60

Figure 1. Polar coordinate system for spherical detached shock waves.

to specifically defined laws. A single value can be obtained through a linear intersection of the arc. We hypothesize the use of a curve ratio from the center point of the sphere, sectioned in conical fashion to express shock wave form. Its polar coordinates are expressed in the following equation as:

$$\frac{r}{R} = \frac{P}{1 - \varepsilon \cos \vartheta} \tag{a}$$

when $\vartheta = 0°$,

$$\frac{r}{R} = \frac{P}{1 - \varepsilon} \tag{b}$$

and by using substitution in the above equation, we get

$$\frac{r}{R} = \frac{r}{R}\left(\frac{1 - \varepsilon}{1 - \varepsilon \cos \vartheta}\right) \tag{1}$$

or

$$\frac{r}{r} = \frac{1 - \varepsilon}{1 - \varepsilon \cos \vartheta} \tag{2}$$

Differential equation (1) can be used to get shock wave inclination β or the corresponding relationship of polar coordinate angle θ

$$\lg \beta = \frac{\varepsilon - \cos \vartheta}{\sin \vartheta} \tag{3}$$

Using the slope of the shock wave to create a relationship of post- M shock wave values where M-post = 1, we can obtain post sonic shock wave polar coordinate angle θ* and ε, and their relationship is as expressed below:

$$\sin \vartheta^* = \varepsilon \cos \beta^* \left\{ \sin \beta^* - \sqrt{\sin^2 \beta^* - (1 - \frac{1}{\varepsilon^2})} \right\} \tag{4}$$

so we have

$$\sin \vartheta^* = \sqrt{\frac{2 - \varepsilon}{4\varepsilon} \left(1 - \frac{3 - \varepsilon}{\varepsilon - 1.0}\right)\left[1 - \sqrt{1 - \frac{16}{(\gamma - 1)M^2 - (3 - \gamma)^2}}\right]} \tag{4a}$$

From equations (1), (3) and (4), we can see: r_o/R and ε are both following the quantitative changes of the influx Mach number values M_∞.

61

When $M_\infty \to \infty$ $\dfrac{r}{R} = \dfrac{r}{R} = 1$, $\xi = 0$

When $M_\infty \to 1$

3. AN.ANALYSIS OF THEORY AND EXPERIMENTAL RESULTS

For an analysis, we are first concerned with the calculated
values for δ/R and θ^*. We start out with the experimental results
and several test formulas, and we selected $\xi = 1/\sqrt{M^2 - 1}$ to make a
self changing variable. By tracing the variables δ/R and θ^*, we
see that they follow the changes along the curves ξ, and they can
be differentiated in Figures 2 and 3. From the figures, we can see:
after using ξ to create an abscissa, in the time of $M_\infty \to 1$, we can
clearly observe the current variational results for all trends of
δ/R and θ^* as they follow the numeric changes of the M_∞. In
Figure 2, as an example, the results for δ/R seem to appear as
"one objective to find, three paths to take". The "one objective"
is for the various results after $M_\infty > 1.5$ to fall in place. It
seems clear that in hypersonic velocity ranges, theory and test
results coincide in excellent fashion. The "three paths" are for
the numeric values calculated after $M_\infty < 1.3$, the test results, and
the test formulas, in all three groupings which have relatively
great differences across their range of results.

The first group of results (5) are taken as wind tunnel
experimental value substitutions, and the test equation can be
expressed as:

$$\frac{r}{R} = \frac{4}{3} \cdot (M_\infty - 1)^{-\frac{1}{2}} \tag{5}$$

These results, at $M_\infty > 1.2$ [8] and a few numeric calculation
results seem to coincide favorably well. At $M_\infty = 1.05$, the results
of other calculations are similar.

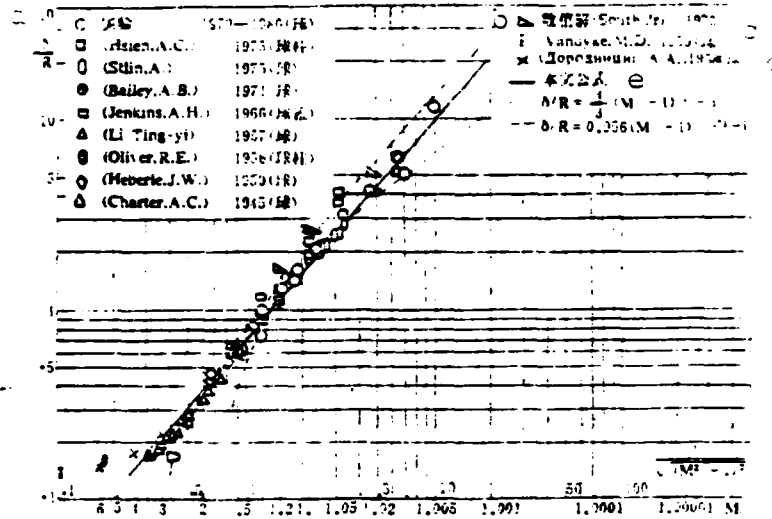The second group of results substituted for the wind tunnel

62

Figure 2. Spherical detached shock wave distance
following numeric changes in values for M_∞.
a--experimental; b--numeric solution; c,d--sphere
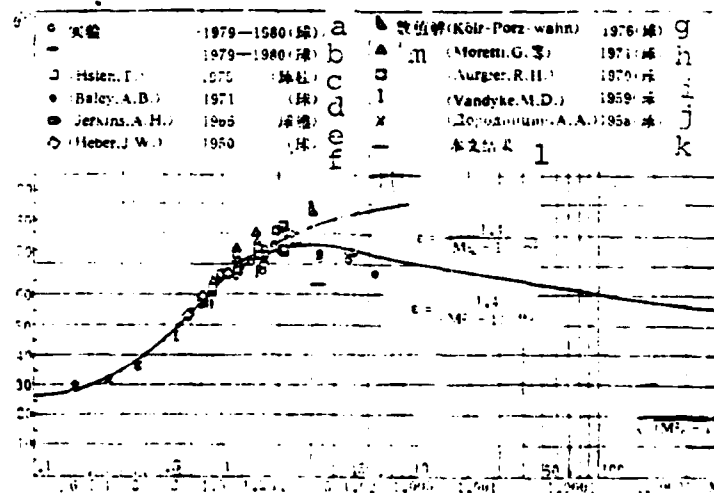e--formula of this document

Figure 3. Post-sonic shock wave positions following
changes in the values for M_∞.
a,b,d,f,g,h,i,j,k--sphere; c,e--spherocylindrical;
l--results of this document; m--numeric solution

63

(1), (7), also have a simple test equation that can be used:

$$\frac{r_2}{R} = 0.356(M_\infty - 1)^{-\cdots}$$
(6)

In the range $M_\infty = 1.05 \sim 1.4$, the aforementioned results from (1),
(7), (8) and (9) are put in the numeric calculation results and
they compare very closely.

The third group, for (10) and (4), are ballistics range results
and substituted wind tunnel results. When $M_\infty > 1.05$, they compare
very closely to the results obtained from the firsg group. When
$M_\infty < 1.05$, the outcome falls somewhere between the results from
the first and second groups. Based on the fact that the ballistics
range equipment is clearly used only as a comparison flow field in
lieu of actual flow and its unique characteristics, we recognize
that the third group of results run counter to the true trends of
change for δ/R which follow the variations in M_∞. Furthermore,
the reason for creation of the third group of results is as follows:
within the vicinity of $M_\infty \cong 1$, calculation of numeric values and
experimental results of wind tunnel measurements are both very
difficult to accurately ascertain. For the many various types of
mistakes that could be made in obtaining the results, a self
correcting evaluation result was needed to prove accuracy. The
utilization of the Mach number counter flow-field results were
assimilated for a composite comparison.

As a foundation for the third group of results, we chose the
following:

$$\varepsilon = \frac{1.4}{(M_\infty - 1)^{\cdots}}$$
(7)

$$\frac{\delta}{R} = 0.46\varepsilon^{\cdots}$$
(8)

By using formulas (1), (2), (7) and (8), we can calculate δ/R, δ,
r/r_o, and r/R for a comprehensive examination of the results com-
pared with the variations in the Mach number values. The comparison
conditions for the experimental results and experimental formulas
may not actually reflect the conditions for true flow.

64

4. RESULTS AND DISCUSSION

Figures (2), (3), (4), (5) and (6) differentiate between the various value changes of δ/R, $\theta*$, r/r_0 and r/R as they follow relational changes in the M_∞ values. From Figure (2), we can see: the δ/R value calculated using (7),(8) in the range of $1 < M_\infty < 4$ for the third group of results compares very well. In comparison with the various methods currently used, in the vicinity of $M_\infty \approx 1$, the results here in this document actually are at odds with the rules set for the detached shock wave distance which follows changes in the M_∞ values.

From Figure (3), we can see: the results of $\theta*$ within the ranges of $1 < M_\infty < 4$, obgained in formulas (7) and (4) in the third group of equations compare very well. They also point out a few important manifestations. Foremost, at $M_\infty \approx 1$ vicinity, the value of $\theta*$ is very sensitive. The differences in variational ε can greatly influence the results of calculation. For example, if we first use formula (7) and the variational ε as expressed in the example formula below:

$$\varepsilon = \frac{1.4}{(M_\infty^2 - 1)^{\cdot}}$$

(9)

we can start our comparison. From Figure (3), one can see that the obtained value for $\theta*$ in formulas (7) and (8), within the range of $M_\infty > 1.2$, is pretty much the same. However, at $M_\infty < 1.05$, there is a great discrepancy. The variational ε obtained in formula (7) showed $\theta*$ results from the third group. Furthermore, with the variation from formula (9), at $M_\infty = 1.01$, $\theta*$ cannot be solved at all. This occurrence could explain why, at conditions of hypersonic velocity, the calculation methods show a wide range of difference in their results, especially at $M_\infty < 1.05$, where it seems to be most difficult to figure. This is the reason the shock wave form does not accurately follow the rules for changes in the M_∞ values.

Additionally, the formulas in this document obtained values for $\theta*$. At $M_\infty \rightarrow 1$, there is a gradual decrease, and at $M_\infty =$

65

1.000001, $\theta*$ 54°. It along with formula (11) linear flow stream at M_∞ = 1 range, accounts for even linear flow of the sphere at sonic speeds. From the values for $M_\infty \to$; θ $R \to$ and $\cdots$, we can solve for the linear course at sonic velocity. When $M_\infty \to$, the detached body of the shock wave stabilizes to that of the shock wave, and the flow following the wave is subsonic. When the shock wave is in extension, it is limited by the value of the Mach number, and the flow around it is hypersonic. As a result, the shock wave must have a sonic point along its curve, as well as a value for $\theta*$ < 90° when values $M_\infty \to$ 1 are present. Also, when $M_\infty \to$ 1, there is no limit to the distance of the physical plane of the shock wave. This is because as $M_\infty \to$ 1, the sonic points along the shock wave are in a forward position.
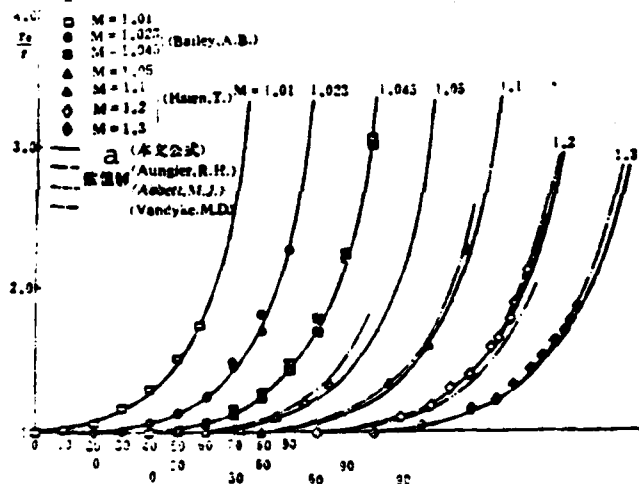

Figure 4. Comparison of results for r/r_o following the changes for θ.
a--formula of this document.

From the calculations of r/r_o obtained in formulas (2) and (7), Figure 4 shows experimental results and numeric figures that coincide in excellent fashion. We should point out that the r_o/R values are counter to the results for variation ε. Figures (5) and (6) show that within the range of 1 < M_∞ < 4, results of r/R follow the changing values of M_∞. From the figures above, we can see that the numeric solution for it and the experimental results coincide quite nicely.
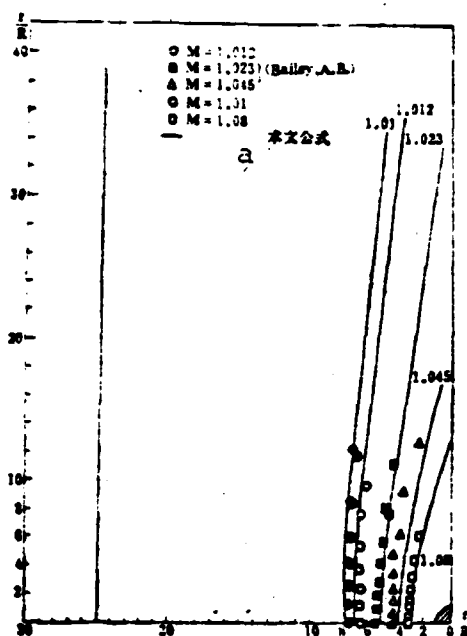
Figure 5. Detached shock
wave form of spherical
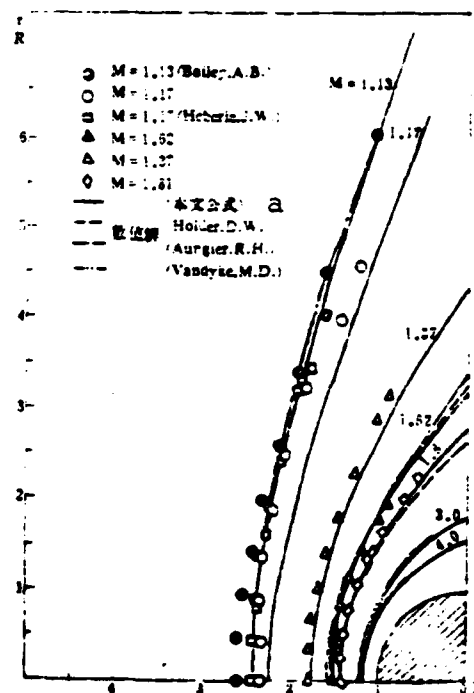body at transonic velocity.
a--formula of this document

Figure 6. Form of detached shock
wave of sphere as it follows the
changes of values for M_∞.
a--formula of this document

In summation of the aforementioned, this document provided a
formula for calculations within the range of $1 < M_\infty < 4$. Within
the vicinity of $M_\infty \cong 1$, actual comparisons are at odds with the
changing M_∞ values which the spherical detached shock wave should,
by rule, follow. The results can be applied to slotted wall inter-
ference in transonic wind tunnels and in observations of experimental
booster flow fields. It is also applicable to numeric calculations
and problem solving analyses methodology which provide results
used in making comparisons. In regard to spherocylindrical and
semi-conical spheres of a < 8°, calculations of di-sonic velocity
detached surface shock wave bodies and experimental results coincide
favorably well in comparisons.

The author would like to express his sincere appreciation to
Professor Lin Tongjia for his guidance.

BIBLIOGRAPHICAL REFERENCES

[1]   Hsien, T., AD-A018157, (1975).

[2]   Zheng Zhichu, Jiang Yangqi, Fei Chong, Journal of Mechanics, 16,2 (1984).

[3] Bailey, A. B., & Miller, D. E., AIAA J. Vol. 19, No. 2, 245(1981).

[4] Bailey, A. B., & Kock, K. E., AD-721208, (1971).

[5] Heberle, J. W., NACA TN 2000, (1950).

[6] Vandyke, M. D., NASA TR R-1, (1959).

[7] James, D. J., AD-A014005.

[8] Aungiek, R. H., AFWL-TR-70-1b, (1970).

[9] South, J. Jr., Proc. of AIAA Comp: Fluid-Dyn Cof.

[10]   Zheng Zhichu, Jiang Yangqi, Wang Jiudun, et al., Journal of Mechanics, 13, 6, (1981).

[11]   Lin, T. C. and Jia Zhenyus, proc. India Acad. Sci. (Eng. Sci) Vol. 4, pt. 3 (1981)

ON DETACHED SHOCK WAVE OF SPHERE MOVING
WITH TRANSONIC VELOCITIES

Zheng Zhichu

(Institute of Mechanics, Academia Scienca·

Abstract

In recent years, there has been an increased interest in the shock shapes about blunt bodies at $M_\infty \cong 1$. The experimental data which were obtained by testing the sphere in ballistic range facility have been analyzed and a signle expression for the shock wave profiles of sphere is presented in this paper. The polar form of this equation is $\frac{r}{R} = \left(1 + \frac{\delta}{R}\right)\left(\frac{1 - \epsilon}{1 + \epsilon \cos^2}\right)$, where dimensionless value of shock detachment distance $\frac{\delta}{R}$ and variation ϵ are function of uniform stream Mach number M_∞. In the $1 < M_\infty < 4$ range, especially at $M_\infty \cong 1$, dimensionless quantities $\frac{\delta}{R}$, $\theta^\bullet$ and $\frac{r}{R}$ which were calculated by equation given in this paper show excellent agreement with free flying data. Also, this equation can be extended to calculate the shock wave profiles of hemisphere-cylinder and spherically blunted cones (half angle $a < 8^\circ$) Furthermore, results in this paper can be extended to study the wall disturbance and test section flow field in transonic wind tunnel.

FINITE DIFFERENCE COMPUTATIONS FOR RADIAL WING FLOW IN A TRANSONIC TWO DIMENSIONAL SLOTTED WALL WIND TUNNEL

Zhang Naiping

(Northwestern Polytechnical University)

1. FOREWORD

Experimental data in a wind tunnel is influenced by a great many factors, chief among which is the influence of slotted wall interference. This is a very serious factor in a transonic velocity field. By using a di-slotted or quadra-slotted transonic velocity wind tunnel duct, we can cause a large reduction of this particular type of interference. However, when the Mach number is relatively high, it makes little difference whether in theoretical research or experimentation because it is just as difficult to cope with the interference in either case.

The classical tunnel wall interference theory considers the influence of compression characteristics in linear subsonic velocity as its foundations. However, when the airfoil surface is primarily in hypersonic velocity fields, a linearized theory cannot accurately provide pressure values. Moreover, the shock wave displacement created by influences of the tunnel wall cause changes to occur in the pressure coefficients. Also, a linearized theory cannot account for these changes in the form of an equation.

Here and abroad, we have already applied the finite difference method and relaxation techniques in order to find solutions for radial wing flow. It has also been used within radial wind tunnels for solutions to airfoil flow problems [1,2,3] mainly in cavity wall applications. This document makes use of these methods to calculate the upper and lower slotting bypass flow at transonic velocity for radial wings in a bypass wind tunnel. The transonic

wind tunnels in the Research Institute of Aerodynamics and Gas-dynamics at Stuttgart University (IAG) 260x700 mm^2 and in the Institute of Aerodynamics at Northwestern Polytechnical University, 100x300 mm^2, were chosen as the two computational examples. Only blockage interference conditions at zero angle of attack are calculated herein.

2. EQUATIONS OF VELOCITY POTENTIAL AND BOUNDARY CONDITIONS

The calculations of this document use the applied two-dimensional transonic velocity small perturbation velocity potential equation, which is

$$(1-M_\infty^2 - \frac{k+1}{U_\infty} M_\infty^2 \varphi_x)\varphi_{xx} - \varphi_{yy} = 0 \tag{1}$$

This equation is a mixed non-linear equation. After application of the small perturbation conditions, we have

$$1 - M_\infty^2 - \frac{k+1}{U_\infty} M_\infty^2 \varphi_x = 1 - M^2 \tag{2}$$

and herein, M is the primary Mach number.

After solving equation (1), all of the necessary boundary conditions for the wing are expressed as:

$$(\varphi_y)_{u,0} = U_\infty \left[\left(\frac{\partial F}{\partial x} \right)_{u,l} - a \right] \tag{3}$$

In the equation, F(x) is a function of the wing exterior surface; lower coordinate, u, 0 differentiates among expressions of lower and upper wing surface. Furthermore, the Kutta boundary conditions are

$$\varphi_x(x, +0) = \varphi_x(x, -0) \tag{4}$$

$$\varphi_y(x, +0) = \varphi_y(x, -0) \tag{5}$$

In the equations, +0 and -0 are differentiated to express upper and lower placement of wing trailing edge flow expansion velocity potential. For example, if H replaced the trailing edge, then we would have

$$\tag{6}$$

$$\varphi(x, +0) - \varphi(x, -0) = \varphi(x_H, +0) - \varphi(x_H, -0) = \Gamma$$

Upper and lower slot conditions in the wind tunnel can be written as

$$c_i \varphi - c_z \frac{\partial \varphi}{\partial x} - c_i \frac{\partial \varphi}{\partial y} - c_i \frac{\partial^i \varphi}{\partial x \, \partial y} = 0 \tag{7}$$

Equation (7) includes different types of boundary conditions in the wind tunnel. In regards to the slotted wall adhesion flow, we have $c_i = 0, c_i = 1, c_i = 1/R, c_i = l,$ and the above equation would be written as

$$\frac{\partial \varphi}{\partial x} + \frac{1}{R} \frac{\partial \varphi}{\partial y} - l \frac{\partial^i x}{\partial x \, \partial y} = 0 \tag{8}$$

$$l = \frac{d}{\pi} \ln \csc \left(\frac{\pi}{2} \frac{t}{d} \right) \tag{9}$$

In this equation, l is a slot-width t and interval d includes its relevant parameters. In regards to the principles of a slotted wall wind tunnel, we can approximate the boundary conditions as:

$$\frac{\partial \varphi}{\partial x} + l \frac{\partial^i \varphi}{\partial x \, \partial y} = 0 \tag{10}$$

The above equation may also be written as

$$\frac{\partial}{\partial x} \left(\varphi + l \frac{\partial \varphi}{\partial y} \right) = 0 \tag{11}$$

The integral equation above applies upper field vernier boundary conditions, and we have

$$\varphi - l \frac{\partial \varphi}{\partial y} = 0 \tag{12}$$

wherein we may get an approximate integral form for the boundary conditions.

The upper and lower field vernier boundary conditions can be reviewed in bibliographical reference [1]. If the wing in experimental stages is placed in a non-symmetrical form, slot gap interval can be differentiated using H_1, H_2 as expressions. When symmetrically placed, we would use the expression $H_1 = H_2 = H/2$. We also have $(\varphi_i)_{i,i} = -(\varphi_i)_{i,i} = \varepsilon_{ii}$. Upper and lower vernier field conditions are

$$\varphi_{i,i} = \int \begin{cases} \varepsilon_i (H_i + y) \\ \text{or } \varepsilon_i \left(\frac{H}{2} + y \right) \end{cases} \tag{13}$$

Issue 3   Zhang Naiping: Finite difference computations for
                            airfoil flow in two dimensional transonic slotted
                            wall wind tunnel

$$\varphi_{1,l} = \begin{cases} \begin{cases} -\varepsilon_0(H_1 + y) + \Delta\varphi_0 \\ c^- \quad -\varepsilon_0\left(\dfrac{H}{2} + y\right) + \Delta\varphi_0 \end{cases} \text{upper vortical} \\ \\ \begin{cases} \varepsilon_0(H_1 + 2H_1 - y) + \Delta\varphi_0 \\ \text{or } \varepsilon_0\left(\dfrac{3}{2}H - y\right) + \Delta\varphi_0 \end{cases} \text{lower vortical} \end{cases} \tag{14}$$

$$\begin{cases} \Delta\varphi_0 = \varphi_{l,1} - \varphi_{1,1} \\ \Delta\varphi_2 = \varphi_{l,l} - \varphi_{1,l} \end{cases} \tag{15}$$

$$\begin{cases} \varepsilon_0 = \dfrac{1}{2(H_1 + H_2)}\left(\varphi_{N,l+1} - \varphi_{N,l-1} - \Delta\varphi_2 + \Delta\varphi_0\right) \\ \text{or } \bar\varepsilon_0 = \dfrac{1}{2H}\left(\varphi_{N,l+1} - \varphi_{N,l-1} - \Delta\varphi_0 + \Delta\varphi_0\right) \end{cases} \tag{16}$$

In the above equations, lower coordinates jt+0 and Jt-0 replace
upper and lower vortical surfaces.

3. CALCULATION PROCESS

Equation (1) is a mixed difference, non-linear form partial
differential equation. Within the field of flow, we must first
carry out a velocity discrimination at each individual mesh point.
In regards to subsonic and sonic velocity points ϕ_x and ϕ_{xx} use a
central differences equation. For those points at hypersonic
velocities, we use rear-oriented single precision differences.
Aside from the field of flow boundary conditions, ϕ_{xx} is also taken
from among central differences. With the line relaxation parallax
y, the difference equation matrix coefficients take on a tri-
dimensional linear equation form which we can use as a tracking
method to find our solution.

The slotted wall boundary conditions ϕ_{xx} in the central
difference equation embody the exterior of the slotted wall,
namely the unspecified points (i,j) and (i,j+1). From the
method cited below, we can take these unspecified points and obtain
values for velocity potential. In regard to the upper surface of
the slotted wall, we have

$$(\varphi_{xx})_{i,l} = \frac{\varphi_{i,l+1} - 2_{i,l} + \varphi_{i,l-1}}{\Delta y^2} \tag{17}$$

$$(\varphi_t)_{i,j} = \frac{\varphi_{i,j+1} - \varphi_{i,j-1}}{2\Delta y} \tag{18}$$

From the $\varphi_{i,j}$ value in these two equations, we get

$$(\varphi_{tt})_{i,j} = \frac{2}{\Delta y^2}(\varphi_{i,j+1} - \varphi_{i,j}) - \frac{2}{\Delta y}(\varphi_t)_{i,j} \tag{19}$$

Herein, for the lower surface of the slotted wall, we have

$$(\varphi_{tt})_{i,j} = -\frac{2}{\Delta y^2}(\varphi_{i,j} - \varphi_{i,j-1}) - \frac{2}{\Delta y}(\varphi_t)_{i,j} \tag{20}$$

with the slotted wall boundary conditions (12) substituted in (19) or (20), we have

$$(\varphi_{tt})_{i,j} = \frac{2}{\Delta y^2}(\varphi_{i,j-1} - \varphi_{i,j}) - \frac{2}{\Delta y \cdot l}\varphi_{i,j} \tag{21}$$

$$(\varphi_{tt})_{i,j} = \frac{2}{\Delta y^2}(\varphi_{i,j} - \varphi_{i,j}) + \frac{2}{\Delta y \cdot l}\varphi_{i,j} \tag{22}$$

With identical wall boundary conditions, for the wing upper and lower surfaces, we can obtain

$$(\varphi_{tt})_{i,j} = \frac{2}{\Delta y^2}(\varphi_{i,j+1} - \varphi_{i,j}) - \frac{2}{\Delta y}(\varphi_t)_{i,j} \tag{23}$$

$$(\varphi_{tt})_{i,j} = \frac{2}{\Delta y^2}(\varphi_{i,j} - \varphi_{i,j-1}) + \frac{2}{\Delta y}(\varphi_t)_{i,j} \tag{24}$$

In the two equations above, $(\varphi_t)_{i,j}$ and $(\varphi_t)_{i,j}$ can be substituted into equation (3).

Due to the line relaxation axis for parallax y, each mesh point's difference equation can only emcompass three unknown velocity potential points, so

$$-a_i \varphi_{i,j-1} + b_i \varphi_{i,j} - c_i \varphi_{i,j+1} = d_i \tag{25}$$

In the equation, coefficients a_i, b_i, c_i, d_i are already known values.

From the small perturbation hypothesis, we can use the following for the calculation of the pressure coefficients:

$$C_p = -\frac{2\varphi_z}{U_\infty} \tag{26}$$

We can use a precision formula to calculate pressure distributions along the wing surface:

$$C_p = \frac{2}{k M_\infty^2}\left\{\left[1 - (k-1)M_\infty^2\left(\frac{\varphi_x \cos\alpha}{U_\infty} + \frac{\varphi_x^2}{2U_\infty^2} + \frac{\varphi_y \sin\alpha}{U_\infty} + \frac{\varphi_y^2}{2U_\infty^2}\right)\right]^{\frac{k}{k-1}} - 1\right\} \tag{27}$$

The calculations were performed using the Qitu Jiate University CDC 6600 computer.

73

4. CALCULATION RESULTS

The calculations for the IAG 260x700 mm^2 wind tunnel were for a non-symmetrical model. The intervals for the upper and lower slots in the model were separated at 400 and 300 mm^2. Lift was for a zero angle of attack. The primary purpose of this document was to calculate blockage interference at zero angle of attack.
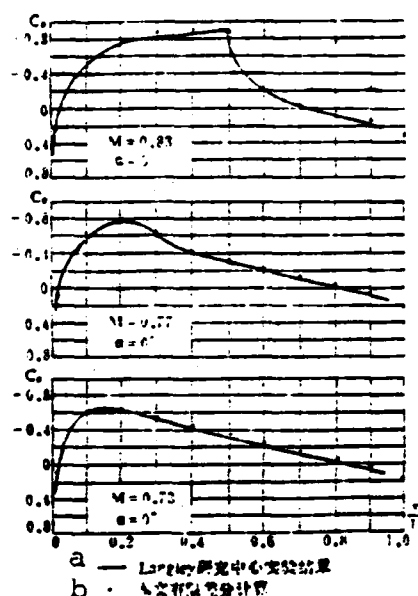

Figure 1a. Pressure distribution curves for a NACA 0012 airfoil at differing Mach nos. a--Langley Research Center test results; b--finite difference calculations of this paper
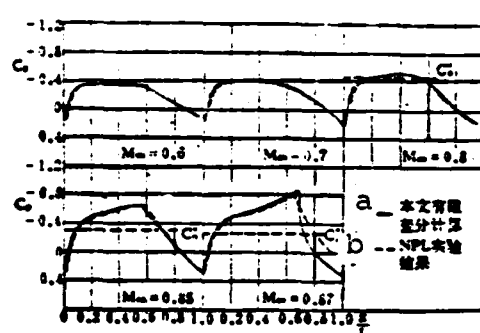

Figure 1b. Pressure distribution curves for a RAE 104 airfoil at differing Mach numbers.
a--finite difference calculations of this paper;
b--NPL lab results

A RAE 104 airfoil of 100 x 300 mm^2 was used in the Northwestern Polytechnical University wind tunnel. A NACA 0012 airfoil was used in the IAG wind tunnel. The calculation results of this document were compared to experimental results from the NPL (National Physical Laboratory) in England and from Langley Research Center in the United States.

Figure 1a points out the pressure distribution calculation results of Mach 0.73, 0.77 and 0.83 for the NACA-0012 airfoil. From the figure, we can see that, aside from when M = 0.83, other Mach value (0.58, 0.64, 0.68 results were not included in the research article) results and those from the Langley Research

74

Center compare favorably well. Clearly, the IAG wind tunnel in the range of these Mach values has the least blockage interference. The calculations in this document are also equally reliable.

Figure 1b points out the pressure distribution calculation results at Mach 0.6, 0.7, 0.85 and 0.87 for a RAE 104 airfoil. Moreover, the NPL linear flow results are used for making comparisons. Aside from the post shock wave pressure distributions when M = 0.87, our calculation results compared very closely to their experimental results.
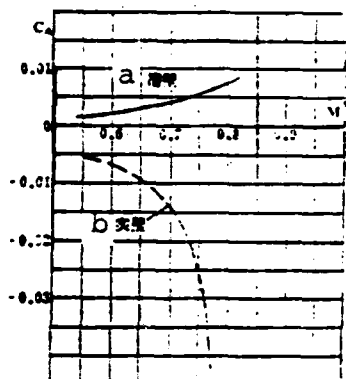

Figure 2. Coefficients of biased zero lift as produced in non-symmetrical slotted wall.
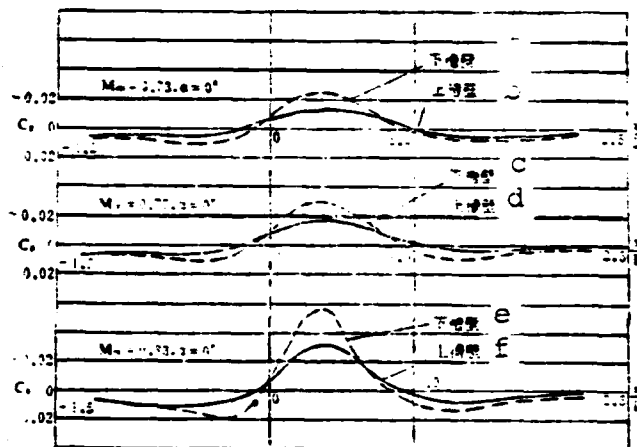a--slotting;
b--experimental

Figure 3. Pressure distribution curve for upper and lower wind tunnel slotting.
a,c,e--lower slot; b,d,f--upper slot

Figure 2 shows a non-symmetrical slotted wall, with differing Mach numbers and the wall bypass flow and bias zero lift coefficients. From the figure, we can see that when the Mach number is increased, the bias lift coefficient produced on the two wall surfaces is also increased. Moreover, the two surface areas are larger. However, when the bias quantity for the test wall is produced, the previously mentioned interference becomes quite severe.

Figures 3 and 4 differentiate the IAG and Xian wind tunnel upper and lower slotting pressure distributions. In the former, the slotting is non-symmetrical, which causes the upper and lower pressure distributions to be different. The latter is symmetrically slotted, and no matter how large the Mach number is, the upper

and lower slotting pressure distribution calculation values remain
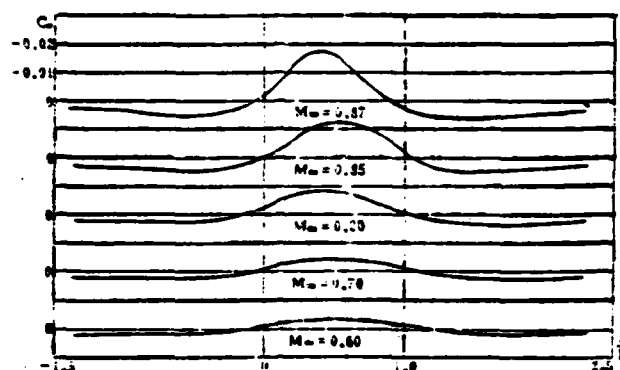symmetrical.

Figure 4. Northwestern Polytechnical University wind
tunnel slotted wall pressure distribution curve.

From the two figures, we can see that for a slotted wall area,
aerodynamic flow in experimental fields with slotted walls is
different from flow in other domains. With different Mach numbers,
the range of aerodynamic flow in experimental stages will also
differ.

BIBLIOGRAPHICAL REFERENCES

[1] Luo Shijun, Mixed Difference Methodology for Normal
     Transonic Velocity Potential Flow, National Industrial
     Press (1977).

[2] Murman. F. M.,AIAA paper. 72-1007, (1972).

[3] Berndt. S.B.,AIAA Journal. 15, 09(1975).

[4] Noonan, K. W. and Bingham, G. J.,NASA Technical paper 1701, (1978).

[5] Krupp, J. A.,Murman, E. M.,AIAA Journal, 10, 7(1972).

[6] Murman. E. M.,Cole, J. D.,AIAA Journal, 9,1 (1971).

[7] Vidal. R. J.,Catlin, P. A.. Chudyk, D. W.,Calspan Report, No. RK-5070-A-3. (1973).

[8] Lock.R. C.: AGARD Repor. No. 575, (1970).

[9] Gothert, B. H.,Transonic Wind Tunnel Testing, (1961).

FINITE DIFFERENCE COMPUTATION OF THE FLOW AROUND AIRFOILS IN TWO-DIMENSIONAL TRANSONIC SLOTTED WALL WIND TUNNEL

Zhang Naiping

(Northwestern Polytechnical University)

Abstract

The transonic flow around NACA 0012 and RAE 104 airfoils in a slotted wall transonic wind tunnel is calculated in this paper with the finite difference method.

A two-dimensional small disturbance velocity potential equation is adopted in this computation. The transonic airfoil wind tunnels in the Institute of Aerodynamics and Gasdynamics of the Stuttgart University and in the Institute of Aerodynamics of Northwestern Polytechnical University in Xian were chosen as two computational examples.

Only the solid blockage interference at zero angle of attack is calculated in this paper. The pressure distributions of the airfoil surface and the slotted wall along the streamwise direction, the additional lift coefficient due to the unsymmetrical set up of the model in the test section are computed.

The calculated results of the NACA 0012 and RAE 104 airfoils are compared with the experimental results of the Langley Reseach Center and those of the National Physical Laboratory in England respectively. In general, the pressure distributions of the airfoil surface were simulated to those of the experiments for the selected Mach Numbers.

END

DTIC

7 — 86